Neutrino Program at the Spallation Neutron Source

ν-SNS

Study Report March 2004

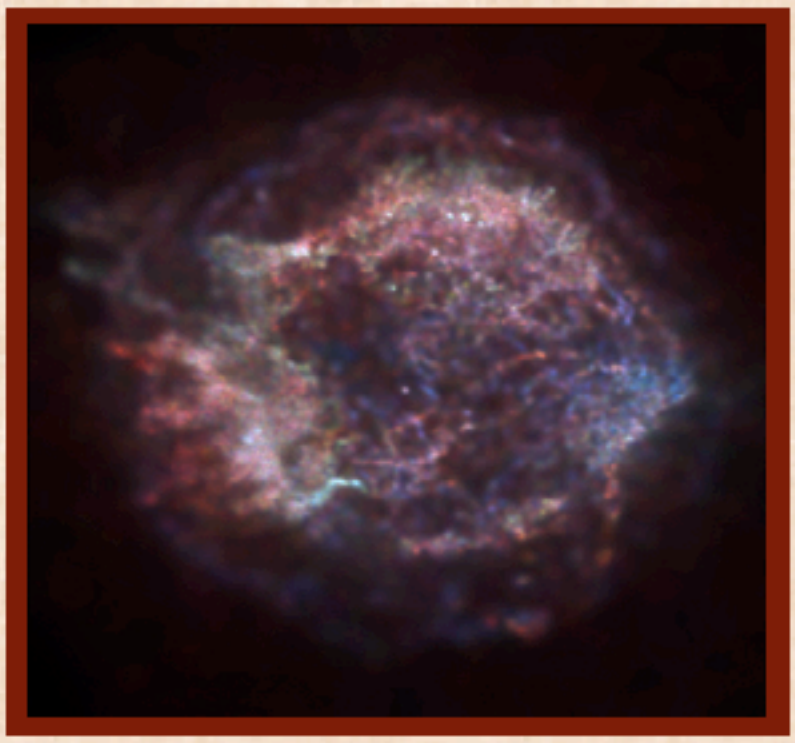

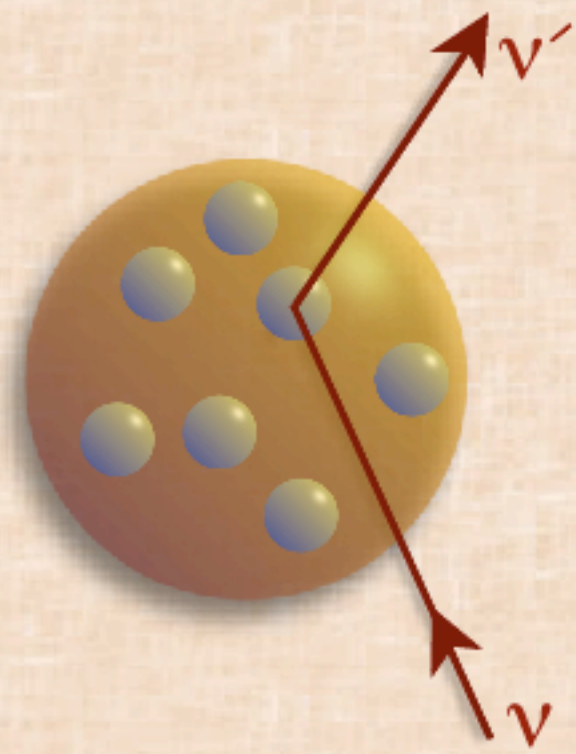

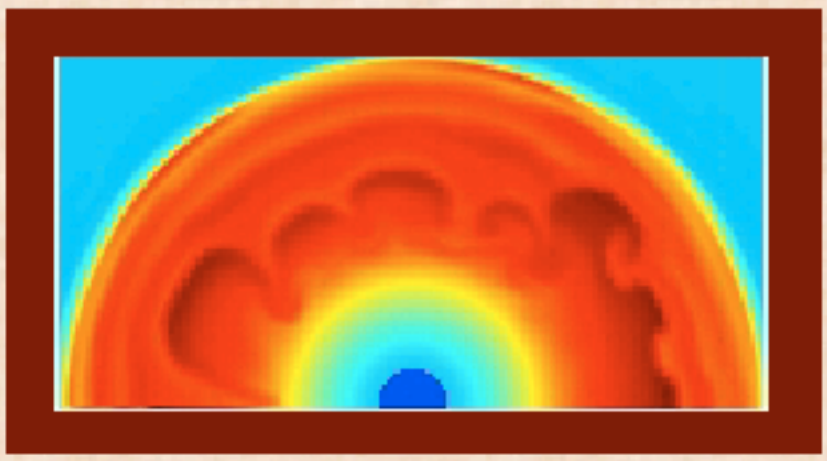

ν-SNS

A Neutrino Facility at the Spallation Neutron Source

Executive Summary

During the last few years, outstanding progress has been made in neutrino physics that has increased our knowledge of neutrino properties with unprecedented speed. This fact is reflected in the recently published *DOE Office of Science Strategic Plan* (Feb 2004) in which half of the major achievements in the field of nuclear physics during the last thirty years are attributed to experiments with neutrinos. Two of the seven highest priorities for the Office of Science listed in the Strategic Plan deal with the importance of understanding the production of the heavy elements in the Universe. Two out of eleven questions raised by the recently published *National Academy of Science Study*, "Connecting Quarks with the Cosmos: Eleven Science Questions for the New Century" are directly related to the experiments with neutrinos. It is clear from just these two studies that neutrino physics will continue to play a major role in the fields of cosmology, nuclear astrophysics, and nuclear structure physics. All of these areas of study will need **high precision** measurements of the neutrino-nucleus interaction at low energy. Yet, neutrino cross sections at low energy have been well measured with accuracy better then 10% on only one nucleus, ^{12}C.

The construction of the Spallation Neutron Source at ORNL provides an extraordinary opportunity to make the high precision neutrino measurements required to satisfy the needs of important astrophysics problems to be addressed over the next few years. As a byproduct the SNS will produce, the world's most intense flux of decay-at-rest neutrinos which have an energy spectrum that fortuitously overlaps with the energy of interest for nuclear astrophysics, supernovae dynamics, and nuclear theory.

Since neutrinos are exceedingly penetrating, a truly non-intrusive facility to study neutrino reactions can be built at the SNS. Preliminary studies show that a shielded neutrino detector enclosure can be built at a distance of 20 meters from the SNS target where the detectors will intercept a neutrino flux more than 10 times greater than was achieved at previous facilities. The anticipated neutrino flux at the SNS facility will allow the measurement of the charged-current neutrino-nucleus cross section for any nuclear target to a statistical accuracy of better then 10% **in one year**!

The neutrino facility will provide for a long-term program of high precision neutrino-nucleus cross-section measurements to meet the needs of astrophysics and nuclear structure physics. It will also provide an ideal location to design and calibrate future dedicated supernovae detector techniques. We initially propose two detectors, designed so that several experiments can be performed with little modification to the detectors. Our present cost estimate for the construction of the shielded neutrino

enclosure with active veto system and two detectors is approximately $7M in FY04 dollars.

The facility will serve as an open user facility beginning operation in 2008, the earliest time high-intensity neutrino flux from the SNS will be available. A multi-institutional collaboration with more than 30 scientists is actively involved in development of a proposal to build the facility.

The attached document provides a high-level **Project Overview**. Following the Overview we have appended expanded versions of some parts of the overview.

List of Appendixes:

Appendix I – Collaboration list
Appendix II - Nuclear Astrophysics at the Spallation Neutron Source
Appendix III - Nuclear Science
Appendix IV – Homogeneous Detector
Appendix V – Segmented Detector
Appendix VI – Veto System
Appendix VII – Neutrino Bunker

ν-SNS

A Neutrino Facility at the Spallation Neutron Source

Project Overview

I. Introduction

The high beam intensity, short duty-factor, and pulsed nature of the Spallation Neutron Source (SNS) at ORNL would enable an exciting program of high statistics neutrino-nucleus cross section measurements. Furthermore, the SNS neutrino spectrum and the neutrino spectrum produced in a supernova explosion are nearly identical. Neutrino-nucleus cross sections are of great importance to the fields of nuclear structure physics and astrophysics; in particular, they would be of immediate use in the study of core-collapse supernova physics.

We propose to build at the SNS a shielded, instrumented enclosure that will hold an initial set of two detectors in order to carry out a long-term program of cross section measurements on a range of appropriate nuclear targets. The tentative name for the proposed facility is **N**eutrinos at the **S**pallation **N**eutron **S**ource, or **ν-SNS**.

At present, only neutrino cross sections on C^{12} have been measured well (~4-10% errors). The only other reported results are for H^2, Fe^{56} and I^{127}, all with ~40% uncertainty. With a facility at the SNS it would be feasible to measure the charged-current neutrino-nucleus cross section for any selected nuclear target species to a statistical accuracy of 10% in one year. Using clever designs that allow reuse of the detector with different target materials it is feasible to develop a true program to measure the cross sections for many nuclear species. Theoretical interest spans the entire range of nuclear species and must be tempered by the realization that neutrino cross sections are exceedingly small (~10^{-41} cm^2) so that even with the prodigious neutrino flux at the SNS, the required target mass is on the order of 10 tons. Therefore, viable target materials must be affordable in large quantity. Based on these considerations an initial three-year program could consist of measurements of the neutrino cross section on lead, iron, carbon, and oxygen with accuracy better than 10%. Future directions would be guided by the results of this initial program and from guidance from astrophysics and nuclear structure theory. Neutral-current measurements and double differential cross section measurements, which are of significant theoretical interest due to the complete lack of experimental data to test theories, may be possible at **ν-SNS** given appropriate detector development, and shielding design.

An appropriate location for the neutrino facility has been found on the floor of the SNS target building and the location has received preliminary approval by the SNS. The neutrino facility will be operated as a User facility for the physics community and the experimental program will be approved and overseen by a Program Advisory Committee. A collaboration of over 30 scientists and a Steering Committee have been established.

II. Scientific Motivation

A Astrophysics

Core collapse supernovae are among the most energetic explosions in our universe, releasing 10^{46} Joules of energy in the form of neutrinos of all flavors at a staggering rate of 10^{57} neutrinos per second and 10^{45} Watts. These explosions almost entirely disrupt stars more massive than 8-10 solar masses. These explosions produce and disseminate into the interstellar medium many of the elements heavier than hydrogen and helium, and are a key link in our chain of origins from the big bang to the formation of life on earth. Core collapse supernovae serve as laboratories for physics beyond the standard model and for matter at extremes of density, temperature, and neutronization that cannot be produced in terrestrial laboratories.

As the name suggests, a core collapse supernova results from the collapse of the core of a massive star at the end of its life. The collapse proceeds to supernuclear densities, at which point the core becomes incompressible, rebounds, and launches a shock wave into the star that is ultimately responsible for the explosion. The shock wave stalls, however, due to several enervating processes, and the shock is believed to be revived in part by the intense flux of neutrinos which emanates from the proto-neutron star at the center of the explosion.

The SNS will produce 10^{15} neutrinos per second from pion and muon decays, and will be the most intense pulsed source of neutrinos on earth. Furthermore, the spectra of supernova neutrinos and the decay-at-rest neutrinos that will be produced at the SNS overlap significantly, as seen in figure 1. The short pulse structure of the SNS beam allows separation of different neutrino species, as shown in figure 2. The availability of such an intense source of neutrinos, with energy spectra matching those emanating from distant supernovae, combined with the strong current interest in neutrinos for supernova science, makes a compelling case for the development of a neutrino-nuclear astrophysics research program at the SNS.

Neutrino-nucleus cross section measurements of relevance to supernova astrophysics fall into three categories: cross sections for: supernova dynamics, supernova nucleosynthesis, and terrestrial supernova neutrino detection.

Supernova Dynamics

Recent studies carried out by the ORNL supernova group have demonstrated unequivocally that electron capture on nuclei plays a major role in dictating the dynamics of stellar core collapse, which sets the stage for all of the supernova dynamics that occur after stellar core bounce and the formation of the supernova shock wave. Past supernova models used naive electron capture rates based on a simple independent-particle shell model for the nuclei in the stellar core. The recent supernova calculations performed by the ORNL group used a "hybrid model”, combining shell model and RPA (random phase

approximation), which better captures the realistic shell structure of the nuclei found in the core and the collective excitations of nucleons in such nuclei during weak interactions such as electron capture. Comparisons of the results from the "hybrid model" with earlier calculations demonstrate that the more realistic electron capture rates lead to quantitative and qualitative changes in the launch radius of the supernova shock wave after stellar core bounce and in the stellar core profiles of density, temperature, and composition. These differences have ramifications for both supernova dynamics and supernova element synthesis.

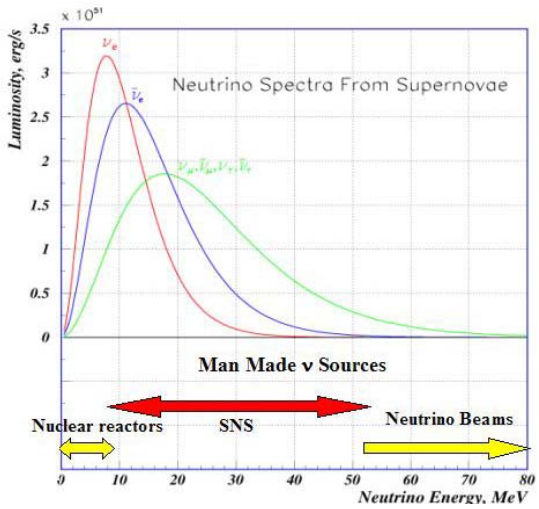

Figure 1. Energy spectrum of neutrinos produced by a supernova (top) and characteristic neutrino energy ranges from various man made sources.

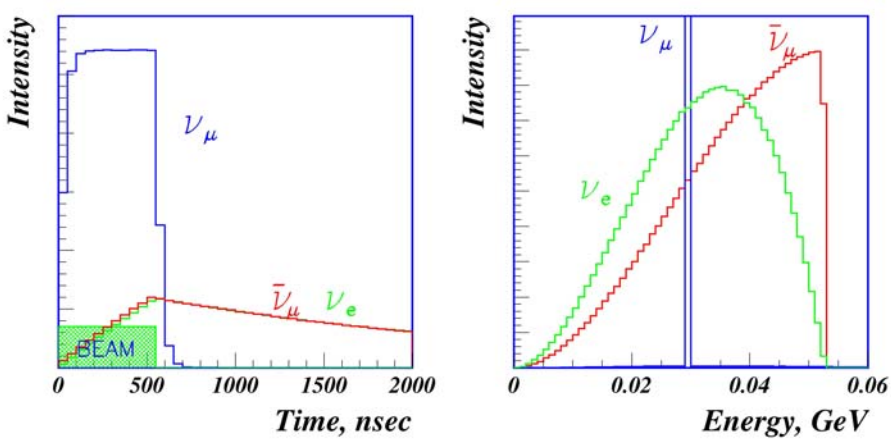

Figure 2. Time structure and energy spectra of different neutrinos species produced at the SNS.

The inverse reactions, electron capture on nuclei and electron-neutrino capture on nuclei, are related. Measurement of the cross section for one of these processes - for example, electron-neutrino capture on nuclei - is tantamount to a measurement of the cross section for the inverse process. It would, of course, be impossible to experimentally measure all of the cross sections that enter the thousands of weak interaction rates needed in realistic simulations of supernovae and supernova nucleosynthesis. Nonetheless, a finite, but strategically chosen set of measurements will validate the fundamental nuclear structure models at the foundation of the thousands of rate computations that are input for supernova models.

Supernova Nucleosynthesis

Nucleosynthesis in core collapse supernovae falls into three basic categories: (1) explosive nucleosynthesis that occurs as the shock wave passes through the stellar layers and causes nuclear fusion through compression and heating of the material, (2) neutrino nucleosynthesis in the ejected layers that occurs as these layers are exposed to the intense neutrino flux emerging from the proto-neutron star, and (3) r-process nucleosynthesis that occurs in a neutrino-driven wind emanating from the proto-neutron star after the explosion is initiated. In all cases, the final elemental abundances produced and ejected are affected through nuclear transmutations by the neutrino-nucleus interactions that occur.

Supernova Neutrino Detection

An incredible wealth of information was derived from the neutrinos emanating from supernova SN1987a that were measured in terrestrial detectors. The ability to detect, understand, and ultimately use the detailed neutrino "light curve" from a future core collapse supernova in our galaxy is integral to developing better supernova models and to using precision supernova models together with detailed astronomical observations in order to cull fundamental nuclear physics that would otherwise be inaccessible in terrestrial experiments. To achieve this will require an accurate normalization of the neutrino flux in a supernova neutrino detector and knowledge of the cross sections and by-products of neutrino interactions in the detector material. From deuterium to lead, a number of nuclei have been proposed and, in some cases, used as supernova detector materials. In all cases, accurate neutrino-nucleus cross sections are essential and currently not available.

B Nuclear Structure

Total neutrino nucleus charged-current cross sections at low energy depend strongly on the charge number of the nucleus. For example the cross section in Pb^{208} is predicted to be 300 times that of C^{12}. Thus, a first measurement on a heavy nucleus may be important to establish the baseline capabilities of the neutrino detection experiment. Furthermore, the charged current reaction cross section induced by ν_e scales nearly as the square of the electron energy and is particularly sensitive to the detailed structure of the induced nuclear excitation spectrum. It is therefore important to either obtain the cross sections directly from the experiment and/or obtain different theoretical estimates in order to determine the theoretical uncertainties and how they affect reaction cross-sections.

Measurements of neutrino-nucleus cross sections open the possibility to study interesting nuclear structure issues related to the weak interaction. One of these involves understanding the ratio of the axial to vector coupling constants. For the Gamow-Teller operator that arises from the low-energy expansion of the weak interaction, one finds that this ratio is modified by the nuclear medium. It is unknown whether other operators in the weak interaction are similarly modified. Using neutrinos from the SNS to probe medium energy strength distributions in ν-A scattering would open the possibility to investigate this fundamental problem. This measurement could be performed on any target material for which low-energy (p,n) experiments are available in order to compare low-energy excitations. Furthermore, a judicious choice of SNS neutrino targets that can simultaneously be developed for inelastic electron scattering at the GSI facility in Darmstadt, could yield simultaneous information on both neutral current (via indirect measurements at GSI) and charged current (at the SNS) neutrino scattering in similar energy windows. This complementary information could be used to evaluate nuclear models that have been developed to predict total neutrino scattering cross sections.

Another interesting research avenue involves the use of nuclear material such as ^{40}Ar to detect rare cosmic ray events and to investigate the properties of neutrinos such as their oscillations, decays, and mass. The experiment, ICARUS at Gran Sasso, is trying to find such rare events. One of the background concerns for ICARUS is low-energy neutrino scattering on ^{40}Ar. This process is very difficult to calculate from nuclear theory due to the cross-shell nature of this nucleus and a direct experimental measurement of the charged-current cross section would be helpful.

The most important nuclear physics inputs for the r-process are the binding energies and lifetimes of nuclei along the r-process path, especially at the so-called waiting points where the flow stagnates, thus producing the major abundances. These waiting points occur in nuclei with 50, 82, and 126 neutrons. An important secondary input is neutrino-nucleus interactions on the waiting point nuclei. Unfortunately, direct neutrino-nucleus measurements on such targets would be impossible, as the material is unstable. However, measurements of neutrino interactions on stable Ni could calibrate nuclear theory in this region, even though the waiting point nuclei are over ten neutron units away from stability. In addition, charged-current information on stable Kr, Rb, and Sr isotopes, which are relatively close to the top of the N=50 r-process path waiting point may prove

very useful for both r-process nucleosynthesis studies and for constraining nuclear models in this somewhat heavier mass region. It is doubtful that the N=126 waiting point nuclei could be addressed in any predictive way even with data from SNS neutrinos on stable nuclei in the region due to their distance from nuclear stability.

III. Proposed Facility

The neutrino detector and shielding enclosure would be located inside the SNS target hall. In discussions with the SNS Target Systems Division we have identified a mutually acceptable location on the north side of the beam line, at a mean distance of ~20m from the spallation target, and at an angle of ~165° relative to the incoming proton beam direction. The available floor space is ~4.5m · 4.5m with a clear height of 6.5m. This location is shown in figures 3 and 4.

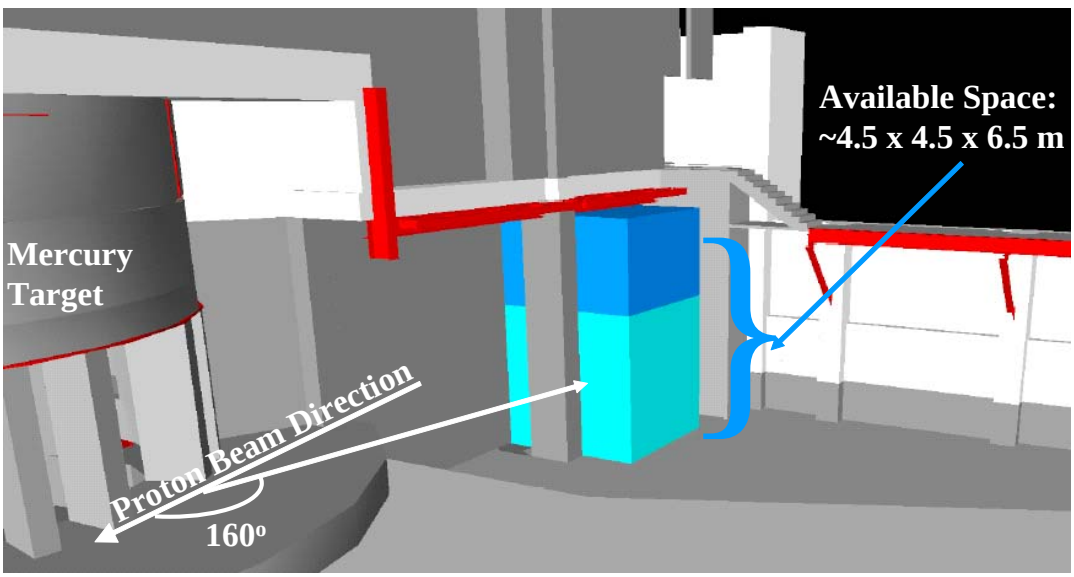

Figure 3. Proposed **ν-SNS** facility location at an angle of ~160° relative to the incoming proton direction and a distance of 21 m from the neutrino source.

At full power (1.0 MW) the SNS will bombard a mercury target with a 1.0 mA, 1.0 GeV proton beam, producing ~0.1 neutrinos per proton in short bursts. The resulting neutrino flux at the detector location will be ~$1.0 \cdot 10^7$ ν/s/cm^2 of each flavor, providing several tens of neutrino interactions per day for a ten ton detector. This must be compared with the cosmic ray muon [or neutron] flux through this volume of ~$2.5 \cdot 10^8$ [$1.4 \cdot 10^6$] events per day. Such cosmic ray events must be suppressed through a combination of the SNS time structure, an active veto counter, and shielding.

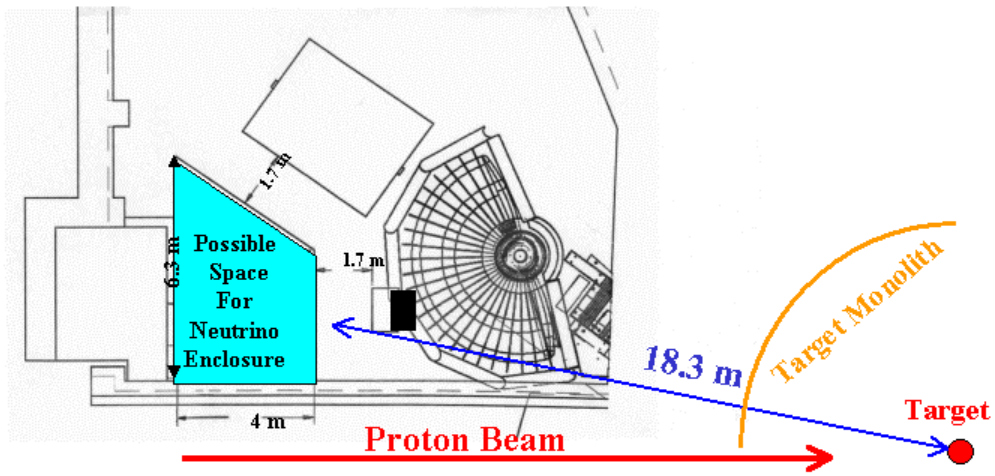

Figure 4. Top view of the proposed ν-SNS facility location relative to the target and the neighboring neutron-scattering instrument.

The SNS time structure (~700 ns proton pulses at 60 Hz) allows us to eliminate a large amount of both types of cosmic backgrounds by turning off the detector except for the small fraction of time during which neutrinos can come from the target. Target neutrinos, which result from the $\pi \rightarrow \mu \rightarrow \nu$ decay chain, will all arrive within several muon decay lifetimes (τ_μ = 2.2 μs). This results in an active time of only $4 \cdot 10^{-4}$ seconds for every second of machine operation, thus reducing the effective cosmic ray muon [neutron] flux through the detector volume to $1 \cdot 10^5$ [$5.6 \cdot 10^2$] events per day.

An active veto system rejects the charged component of the cosmic background. We assume an achievable efficiency of greater than 99% for the veto system that would further reduce the cosmic ray muon flux to below 10^3 events per day. Most of the remaining muons can be rejected by their signature in the detector, but those which produce a neutron in the shielding can be confused with the desired signal of neutrino detection. To a good approximation, we are only concerned with those muons that produce a neutron in the last interaction length of shielding. The observed $\mu \rightarrow n + X$ yield is $4 \cdot 10^{-5}$ n/μ/(g/cm^2), yielding a background rate of ~5.2 events/day coming from neutrons generated in the shielding enclosure by cosmic ray muons which failed to fire the active veto system. This background can be additionally suppressed by a factor of 3 to 5 by using particle identification in the detectors.

Without shielding, the primary cosmic neutron flux is (as discussed above) ~560/day, two orders of magnitude above the irreducible background from cosmic muons. This sets the scale for the thickness of shielding: a steel enclosure, with a 1 m thick roof and 0.5 m thick walls will reduce the primary cosmic neutron flux by two orders of magnitude. Preliminary calculations, incorporating the SNS target and shielding assemblies and materials from nearby neutron scattering instruments show that this shielding, together with benefits from the SNS time structure, is also sufficient to shield against SNS-

generated neutrons for measurements of charged-current neutrino interactions. For measurements of neutral-current neutrino interactions future shielding studies are required when a detailed layout of the closest neutron beam lines becomes available.

Calculations performed by the engineering firm **m+w zander** show that the weight of the required shielding and the detectors is within the load limit of the SNS floor at our desired location. The 3.5m · 3.5m · 5.5m interior space of the facility is sufficient to house two neutrino target/detector systems.

IV. Possible Detectors

Several different types of detectors are being investigated to measure the energy of the neutrino-nucleus interaction byproducts. The two that appear most promising are:

- Segmented detector - a finely-grained or highly segmented tracking detector with the target material distributed in the form of solid cylindrical tubes;
- Homogeneous detector - a liquid-filled tank with close-packed photo detectors on the inner surface that could be operated either as a scintillation detector or as a Cherenkov detector.

A. Segmented Detector

Individual elements of the segmented detector would be composed of a position-sensitive gas proportional counter surrounded by a thin-walled cylindrical tube made of the target element. Signals would be read out from both sides of each individual channel to provide three-dimensional position information. Particle energy is reconstructed from the range of the particle track or from the total number of fired cells. Direction information can be extracted from the reconstruction of the track. In principle, this detector can be constructed in such a way that the detector elements are reusable. When a measurement with one target material is complete the target/detector combinations would be unstacked, the detector elements would be removed and loaded into a new set of target tubes, and the new target/tube combinations re-stacked. As a result, neutrino interactions with different nuclei can be studied with the same detector. This has great benefits for systematic error reduction as well as for long-term ease of operation and reduced cost. Cylindrical tubes of lead, aluminum, and iron are easily obtainable; suitable tubes of many other target other elements can possibly be manufactured as powder contained in a plastic matrix.

Detectors with gas tubes as the sensitive elements have a number of advantages. In general, gas tubes are less expensive than any other materials and do not require an expensive readout system. In addition, the low detector mass eliminates the necessity to statistically separate interactions in the target from the interactions in the detector itself. For electrons in the energy range of a few tens of MeV the energy resolution obtained by measurement of the track length is as good as that obtained by measurement of the sampling energy deposition.

Monte Carlo studies show that a reasonable design for the target tubes would be 1.5 cm diameter tubes with a wall thickness of 0.75 mm. An iron target with a 10 ton fiducial mass would be 2.0 m · 2.0 m and would have 2.0 m long tubes. The total target/detector volume should include an additional 10 cm beyond this fiducial volume to ensure that accepted events are totally contained. This results in a size of 2.2 m · 2.2 m · 2.2 m – or a total of 21,000 2.2 m long target/detector tubes. For an iron target with 10 ton fiducial mass, at a mean distance of 21 m from the SNS spallation target, and with an expected cross section of ~$2.6 \cdot 10^{-40}$ cm^2, the expected neutrino interaction rate is 25 per day. We estimate a detector efficiency of 40%, leading to a signal of ~10 events per day or about 2 thousand events per year.

B. Homogeneous Detector

Some nuclei are difficult or impossible to obtain as solid compounds. It is more efficient to measure such targets (e.g., ^{2}H, ^{12}C, ^{16}O, ^{127}I) in the form of a liquid or an aqueous solution. Therefore we propose to have a second, homogeneous, detector that can be filled with various liquids. The detector would be built as a steel, light tight vessel with a volume of ~27 m^3. Scintillation or Cherenkov light would be detected by ~300 8" PMTs (or other type of photodetectors) mounted on the inner wall.

The first target for this detector would likely be C^{12} (liquid scintillator). The C^{12} cross-section has been previously measured by both KARMEN and LSND, but better data are desired. For the SNS neutrino facility the expected rate is ~10 events per day (3500 events per year) assuming a detection efficiency of 60%. One year of operation at the SNS would yield seven times the total number of events measured by KARMEN after five years of operation. An additional benefit of an early C^{12} measurement is that it will provide a calibration of the SNS neutrino flux. This is critical to provide a systematic accuracy for the measurements that is comparable to the expected statistical precision.

V. Compatibility with SNS operations

As shown of the figure 4, we have identified a location for the proposed neutrino facility that is far away from any existing or future neutron scattering instruments. The proposed facility will have no interference with normal SNS operations.

VI. Schedule

Our experimental schedule is guided by the expectation of full-power beam at the SNS by the end of 2008, at which time we could efficiently begin to commission our detectors. In order to achieve this schedule we need to perform detailed design studies and some R&D in FY05-06; begin detector construction and engineering the shielded enclosure in FY06; erect the shielding enclosure in FY07; and install the detectors in FY08.

VII. Cost

We have made an initial estimate of the construction cost for this facility. There are three main items requiring investment in equipment: the shielded enclosure with an active veto system, and two neutrino detectors. Very preliminary cost estimations in FY04 dollars:

Homogeneous detector	- $1.1M
Segmented detector	- $2.4M
Veto System	- $1.2M
Bunker	- $0.5M
Total	- $5.2M
Contingency	- 40%
Grad Total	**- $7.3M**

This cost includes cost of target materials for the initial sets of measurements. Details of the estimations can be found in attachments.

Since the detectors will be reused for measurements of additional nuclei, the cost for those measurements is limited to the new targets cost. We estimate this cost to be between $500K and $1000K depending of the target material.

VIII. Collaboration

It is our intention that the proposed neutrino facility be operated as a user facility for the neutrino community and that experimental priority be set by an independent Program Advisory Committee. Once the detectors are built, the key issues will be selection of target materials, and the duration of the experimental runs.

On August 28-29th we organized the "Neutrino Studies at the Spallation Neutron Source" workshop at ORNL (**http://www.phy.ornl.gov/workshops/sns2/**). Approximately 40 participants from a dozen institutions attended. The clear consensus was that it is imperative to have such neutrino program, and that SNS is the only place to host it.

The Collaboration is open to all users. There are currently ~ 30 scientists in the Collaboration and a Steering Committee has been established from the User Community. Members of this Committee will provide guidance for the project and each member has taken leadership responsibility for a major part of the project construction.

The following institutions are currently a part of the collaboration:

University of Aarhus
University of Alabama
Argonne National Laboratory
University of Basel
California Institute of Technology
UCSD
Clemson University
Colorado School of Mines
Fermi National Accelerator Laboratory
University of Houston
Los Alamos National Laboratory
North Carolina State University
Oak Ridge National Laboratory
University of South Carolina
Spallation Neutron Source
University of Tennessee
University of Wisconsin

Discussions are actively under way with additional collaborators.

The Steering Committee members and their responsibilities are:

Bunker – Vince Cianciolo, ORNL
Email: vince@mail.phy.ornl.gov, Ph. (865)-574-4712
Theory (Nuclear) - David Dean, ORNL
Email: deandj@ornl.gov, Ph. (865)-576-5229
Liquid Detector – Ion Stancu, Alabama
Email: Ion.stancu@ua.edu, Ph. (205)-348-7777
Segmented Detector – Yuri Efremenko, Tennessee (Project Coordinator)
Email: efremenk@unix.utk.edu, Ph. (865)-574-4706
SNS Integration Liaison – Tony Gabriel, SNS
Email: gabrielta@ornl.gov, Ph. (865)-574-6082
Active Veto – Uwe Greife, Colorado School of Mines
Email: ugreife@mines.edu, Ph. (303)-273-3618
Theory (Astro) – Antony Mezzacappa, ORNL
Email: mezzacappaa@ornl.gov, Ph. (865)-574-6113
Future Experiments – Richard Van de Water, LANL
Email: vdwater@lanl.gov, Ph. (505)-667-6375

Appendix-I

ν-SNS Collaboration

University of Aarhus
K. Langanke

University of Alabama
I. Stancu

Argonne National Laboratory
R.L. Talaga

University of Basel
E. Kolbe

California Institute of Technology
P. Vogel

University of California San Diego
George M. Fuller

Clemson University
B. Meyer

Colorado School of Mines
U. Greife
F. Sarazin

Fermi National Accelerator Laboratory
J. Beacom

Los Alamos National Laboratory
R.L. Burman
W.C. Louis
G. Mills
R. Van de Water

University of Houston
E. Hungerford

North Carolina State University
G. McLaughlin
D. Markov

Oak Ridge National Laboratory
D.W. Bardayan
J.C. Blackmon
F.E. Bertrand
T.V. Cianciolo
D.J. Dean
A.M. Mezzacappa
P.E. Mueller
M.S. Smith
G.R. Young

University of South Carolina
F. Avignone
V. Gudkov

Spallation Neutron Source
G.W. Dodson
T.A. Gabriel

University of Tennessee
Y.V. Efremenko
W.M. Bugg
W.R.Hix

University of Wisconsin
A.B. Balantekin

Appendix-II

Nuclear Astrophysics at the Spallation Neutron Source

The intense neutrino source that is a fortuitous by-product of the Spallation Neutron Source provides a unique opportunity to measure the strength of many neutrino-nucleus interactions that are important in astrophysics. The lives of massive stars lead naturally to bright neutrino sources where interactions between the neutrinos and matter are important. The leading example of this is core collapse supernovae, though two related scenarios, accretion induced collapse, where a white dwarf collapses to form a neutron star (without launching a supernova), and collapsars, where a failed supernova results in a black hole surrounded by a massive accretion disk, may produce similar conditions. We will begin this section by briefly reviewing the core collapse supernova mechanism and the current state of its modeling. We will then discuss the importance of neutrino-nucleus interactions to the supernova mechanism, supernova nucleosynthesis and detection of neutrinos from supernovae.

1 The Mechanism of Core Collapse Supernovae

Core collapse supernovae are among the most energetic explosions in the Universe, releasing 10^{46} Joules of energy in the form of neutrinos of all flavors at the staggering rate of 10^{57} neutrinos per second and 10^{45} Watts. Marking the death of a massive star (mass >8-10 solar masses) and the birth of a neutron star or black hole, core collapse supernovae serve as laboratories for physics beyond the Standard Model and for matter at extremes of density, temperature, and neutronization that cannot be produced in terrestrial laboratories. The 10^{44} Joules of kinetic energy and rich mix of recently synthesized elements delivered into the interstellar medium by the ejecta of each supernova make core collapse supernovae a key link in our chain of origins from the Big Bang to the formation of life on Earth.

The center of a massive star, as it nears its demise, is composed of iron, nickel, and similar elements, the end products of stellar nucleosynthesis. Above this *iron core* lie concentric layers of successively lighter elements, recapitulating the sequence of nuclear burning that occurred in the core during the star's lifetime. Unlike prior burning stages, where the ash of one stage became the fuel for its successor, no additional nuclear energy can be released by further fusion of the maximally bound, iron peak nuclei. No longer can nuclear energy production stave off the inexorable force of gravity. When the iron core grows too massive to be supported by electron degeneracy pressure, the core collapses. This collapse continues until the core reaches densities similar to those of the nucleons in a nucleus, whereupon the repulsive core of the nuclear interaction renders the core incompressible, halting the collapse. Collision of the supersonically falling overlying layers with this stiffened core produces the *bounce shock*, which drives these layers outward. However, this bounce shock is sapped of energy by the escape of neutrinos and nuclear dissociation and stalls before it can drive off the envelope of the

star (see, e.g., [1]). The failure of this *prompt* supernova mechanism sets the stage for a *delayed* mechanism, wherein the intense neutrino flux, which is carrying off the binding energy of the proto-neutron star, heats matter above the neutrinospheres and reenergizes the shock [2,3]. The heating is mediated primarily by the absorption of electron neutrinos and antineutrinos on the dissociation-liberated free nucleons behind the shock. Although four decades of supernova modeling have established this textbook explanation, models of this mechanism frequently fail to produce explosions, thus fundamental questions about the explosion mechanism remain.

The neutrino energy deposition behind the shock depends sensitively on the neutrino luminosities, spectra, and angular distributions in the postshock region. Ten percent variations in any of these quantities can make the difference between explosion and failure in supernova models [4,5]. Thus, accurate multigroup Boltzmann neutrino transport must be considered in supernova models. Past spherically symmetric simulations have implemented increasingly sophisticated approximations to Boltzmann transport: simple leakage schemes, two-fluid models, and multigroup flux-limited diffusion [6,7,8,9]. A generic feature of this last, most sophisticated approximation is that it underestimates the isotropy of the neutrino angular distributions in the heating region and, thus, the heating rate [10,11]. With these limited transport approximations came the possibility that the failure to produce explosions in the past may have resulted from incomplete neutrino transport.

To address this possibility, complete Boltzmann neutrino transport models have been constructed in recent years by several groups [12,13,14,15]. As a class, these models have failed to produce explosions for a range of progenitor masses from 13-40 solar masses. Though the neutrino heating rate is large, because of the stratified temperature structure imposed by spherical symmetry, the heating region is small and the total deposited energy is insufficient to eject the envelope. These models make it clear that the failure of prior supernova models was not the result of inadequate transport approximations. This would suggest that changes in the microscopic input physics (i.e., weak interaction physics and nuclear physics in the Equation of State) and/or initial conditions (i.e., stellar evolution models) are needed and/or that macroscopic effects such as convection, rotation, and magnetic fields are required ingredients in the recipe for explosion.

Multi-dimensional simulations allow investigation of the role convection, rotation, and magnetic fields may play in the explosion. Supernova fluid instabilities fall into two categories: (1) instabilities near or below the neutrinospheres, which we refer to as proto-neutron star instabilities and (2) convection between the gain radius and the shock, which we refer to as neutrino-driven convection. Proto-neutron star instabilities may aid the explosion mechanism by transporting hot, lepton-rich matter to the neutrinospheres, thereby boosting the luminosities at the neutrinosphere. Neutrino-driven convection aids the explosion mechanism by boosting the neutrino heating efficiency, thereby facilitating shock revival.

Within the proto-neutron star (PNS), whose “surface” is defined by the neutrinospheres, a number of fluid instabilities may arise as the result of the lepton and

entropy gradients present. The lepton gradients are established by the deleptonization of the proto-neutron star via electron-neutrino escape near the electron neutrinosphere, whereas the entropy gradients result from the weakening supernova shock. (As the shock weakens, it causes a smaller entropy jump in the material flowing through it.) The development of convection in the proto-neutron star is a radiation hydrodynamic phenomenon, rather than a purely hydrodynamic phenomenon. In this region of the stellar core, neutrinos and the stellar core fluid are coupled. The neutrinos have the ability to equilibrate an otherwise buoyant fluid element with its surroundings in both lepton number and entropy, rendering the fluid element non-buoyant. To date, simulations in this regime have been highly dependent on the assumptions made in constructing the models [16,17,18]. Neutron fingers are another instability that may occur in regions of crossed gradients in lepton fraction and entropy. Neutron fingers are "doubly diffusive" instabilities, stemming from competing efficiencies of lepton number and entropy transport in the core. An early attempt to investigate these effects was made in the simulations by Wilson & Mayle [9]. These one-dimensional models lifted spherical symmetry in an approximate fashion using a phenomenological mixing-length description for neutron finger convection inside the proto-neutron star, which boosted the neutrino luminosities, causing explosions. However, the strength of the neutron finger instability assumed by Wilson & Mayle is controversial, as shown in detailed numerical neutrino equilibration experiments by Bruenn and collaborators [19,20]. Future models, combining full 3D radiation hydrodynamics with improved neutrino-matter interactions, will be needed to assess the strength and importance of PNS instabilities.

Neutrino-driven convection occurs in the region behind the stalled shock but above the gain radius as a result of the entropy gradient that forms as material infalls while being continually heated from below. Models show high-entropy, rising plumes and lower-entropy, denser, finger-like downflows beneath the shock, leading in some cases to successful explosions. In Herant et al. [21], this large-scale convection led to increased neutrino energy deposition, the accumulation of mass and energy in the gain region, and a thermodynamic engine that "ensured" an explosion. In some models by Burrows et al. [22], neutrino-driven convection significantly boosted the shock radius and led to explosions. Recently, Fryer and Warren [23] (using methods similar to [21]) have demonstrated that three dimensional models exhibit convective behavior similar to the two dimensional models. This somewhat surprising preference for large scale convection in both two and three dimensional simulations is possibly explained by hydrodynamic instabilities in the stalled accretion shock [24].

However, multi-dimensional simulations are not guarateed to produce explosions. Janka and Müller [4], using a central adjustable neutrino lightbulb, conducted a parameter survey and concluded that neutrino-driven convection aids explosion only in a narrow luminosity window, below which explosions do not occur and above which neutrino-driven convection is not necessary. In two-dimensional models by Mezzacappa et al. [25], the angle-averaged shock radii do not differ significantly from the shock trajectories in their one-dimensional counterparts, and no explosions are obtained. These two-dimensional simulations implemented spherically symmetric (1D) multigroup flux-limited diffusion neutrino transport, compromising transport spatial dimensionality to implement multigroup transport and a seamless transition between neutrino-thick and

neutrino-thin regions. Most recently, a simulation by Buras et al. [18], coupling 2D hydrodynamics with the ray-by-ray neutrino transport (performing independent calculations of the radiation transport along each radial direction), failed to produce an explosion. In light of the neutrino transport approximations made in all multidimensional supernova simulations to date, next-generation simulations will have to reexplore neutrino-driven convection in the context of three-dimensional hydrodynamics coupled to more realistic multigroup three-dimensional neutrino transport. However, such simulations will only be as accurate as the neutrino matter interactions they include.

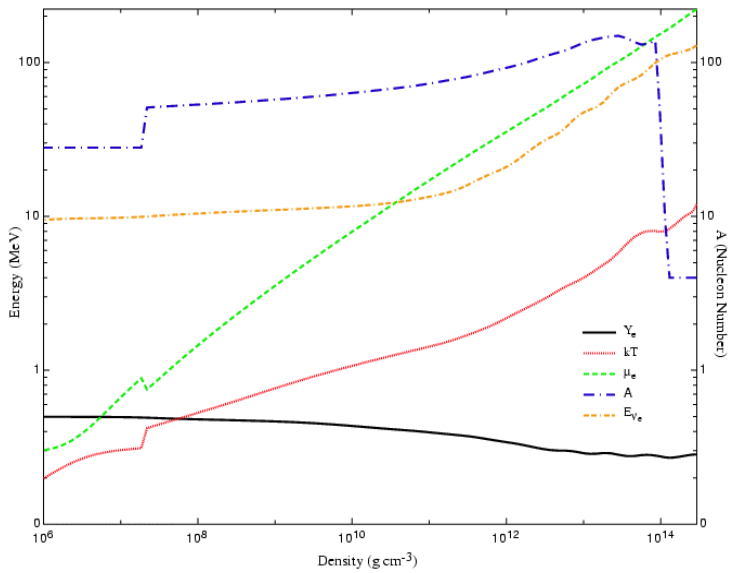

Figure 1: The energy scales and composition as a function of density in the collapsed stellar core at bounce for a 15 M progenitor [26].

2 Neutrino-Nucleus Interactions and Core Collapse Dynamics

While neutrino interactions with shock heated nucleons are the major source of the neutrino heating which drives the delayed shock, neutrino interactions with nuclei are also important before and after the passage of the shock. During the collapse of the stellar core, electrons are captured on heavy nuclei and free protons in the core, producing electron neutrinos that initially escape, *deleptonizing* the core. Where the shock forms in the stellar core at bounce and how much energy it initially has are set by the amount of deleptonization in the core during collapse. Deleptonization would be complete if electron capture continued without competition, but at densities of order $10^{11\text{-}12}$ $g\ cm^{-3}$, the electron neutrinos become "trapped" in the core, and the inverse reactions—charged-current electron-neutrino capture on iron-peak nuclei and free neutrons—begin to compete with electron capture until the reactions are in weak equilibrium and the net deleptonization of the core ceases on the core collapse time scale. The equilibration of electron neutrinos with the stellar core occurs at densities between $10^{12\text{-}13}$ $g\ cm^{-3}$. Figure 1 summarizes the thermodynamic conditions throughout the core

at bounce and displays the temperature, electron fraction (Y_e), electron chemical potential (μ_e), and mean electron neutrino energy ($E_{\nu e}$) in MeV as functions of the matter density. Also shown is the representative nuclear mass (A). The kinks near 3×10^7 $g\ cm^{-3}$ mark the transition to the silicon shell. As the stellar core densities increase, the characteristic nuclei in the core increase in mass, owing to a competition between Coulomb contributions to the nuclear free energy and nuclear surface tension. For densities of order 10^{13} $g\ cm^{-3}$, nuclei with mass >100 dominate. For densities exceeding 10^{14} g cm^{-3} heavy nuclei are replaced by nuclear matter. Figure 2 demonstrates that the nuclear composition shows a wide spread in mass, with species with significant concentrations having masses that differ by 40. Further, Figure 2 also shows that the abundances of nuclei with mass greater than 100 are significant as early as 10^{11}g cm^{-3}. **Thus, cross sections for charged-current electron and electron-neutrino capture on nuclei at least through mass 120 are needed to accurately simulate core deleptonization and to accurately determine the postbounce initial conditions.**

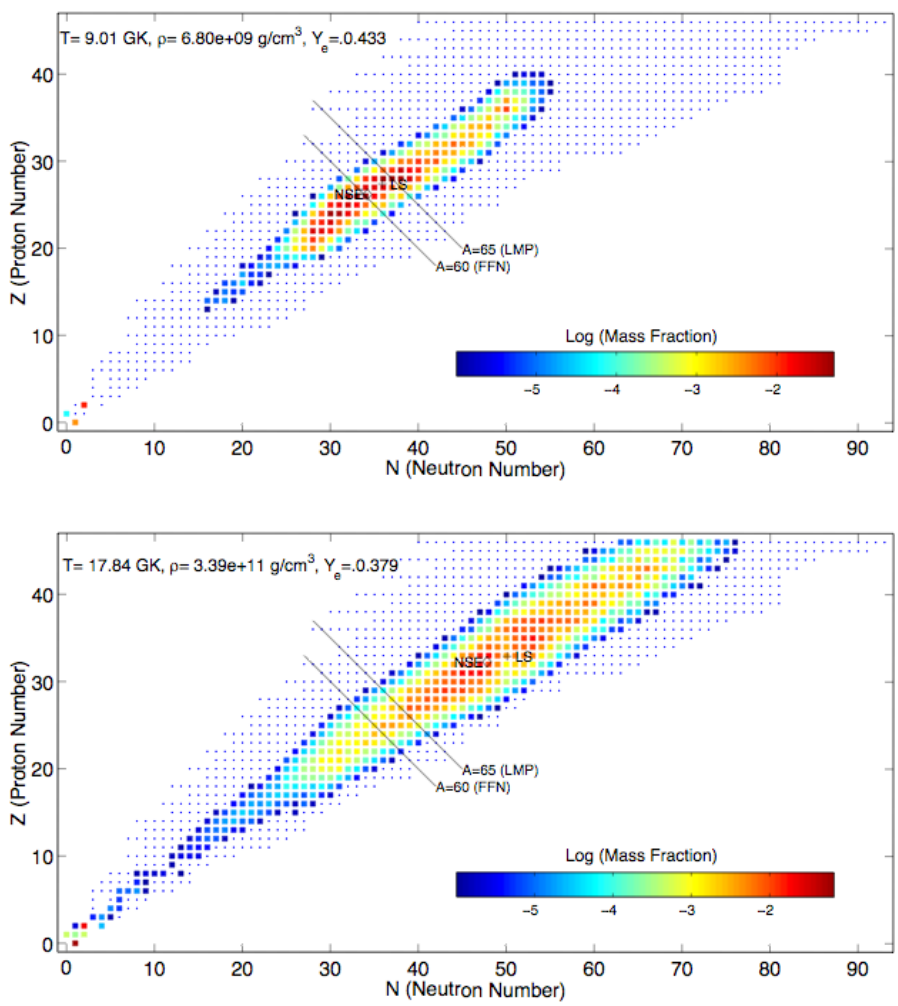

Figure 2: Details of the composition at two points during stellar core collapse [27].

Improved shell model calculations of weak interaction rates for electron capture, positron capture, and β^- and β^+ decays on nuclei relevant for stellar evolution ($45<A<65$) have become available in recent years [28,29]. Heger et al. [26] utilized these new weak reaction rates to improve upon the stellar evolution simulations of Woosley & Weaver (WW95)[30], replacing the weak interaction rates for electron and positron captures and β^- and β^+ decays. The WW95 models used the electron capture rates of Fuller, Fowler, & Newman (FFN) [31] and older sets of beta decay rates [32,33]. The most noticeable effect of these improvements is a marked increase in the electron fraction (Y_e) throughout the iron core before collapse. Because the final size of the homologous core, and therefore the shock formation radius, is proportional to the square of the trapped lepton fraction (Y_l^2) at core bounce [34], it was suggested that the persistence of these initial differences in Y_e throughout collapse should have a discernible (positive) effect on the shock energetics.

For many years, the neutrino emissivity from nuclei developed by Bruenn [7] have served as the standard. Langanke et al. [35] have recently produced electron capture rates for a sample of nuclei with A=66-112 using hybrid, shell-model–RPA calculations. Hix et al. [36] used these rates to develop a greatly improved treatment of nuclear electron capture. To calculate the needed abundances of the heavy nuclei, a Saha-like NSE was used, including Coulomb corrections to the nuclear binding energy [37,38], but neglecting the effects of degenerate nucleons [39]. This improved treatment of nuclear electron capture has two competing effects. In lower density regions, where the average nucleus is well below the N=40 cutoff of electron capture on heavy nuclei, the Bruenn parameterization results in more electron capture than the LMP+hybrid case. This is similar to the reduction in the amount of electron capture seen in stellar evolution models [26] and thermonuclear supernova [40] models when the FFN rates are replaced by shell model calculations. In denser regions, the continuation of electron capture on heavy nuclei alongside electron capture on protons results in more electron capture in the LMP+hybrid case. This produces a marked reduction (11%) in the electron fraction in the interior of the PNS, resulting in a nearly 20% reduction in the mass of the homologous core, which manifests itself at bounce as a reduction in the mass interior to the formation of the shock from 0.67 $M_\odot$ to 0.57 $M_\odot$ in the LMP+hybrid case. A shift of this size is very significant dynamically because the dissociation of .1 solar mass of heavy nuclei by the shock costs 10^{51} erg, the equivalent of the explosion energy. There is also an 11% reduction in the central density and a 7% reduction in the central entropy at bounce, as well as a 10% smaller velocity difference across the shock and quite different lepton and entropy gradients throughout the core. In the outer regions, the higher electron fraction slows collapse, resulting in, for example, reductions of a factor of 5 in density and 40% in velocity in the vicinity of 0.8 $M_\odot$.

These differences in the behavior of collapsing stellar cores illustrate the importance of weak interactions with nuclei. At the onset of collapse, the nuclei of interest are clustered in mass between 50 and 70 along the neutron-rich edge of stability. Throughout collapse, decreasing electron fraction and increasing density pushes the

composition to heavier and more neutron-rich nuclei, including nuclei 4-6 decays away from stability and with masses greater than 100. The KARMEN collaboration pioneered work in this regime, measuring the cross section for $^{56}Fe(\nu_e,e^-)^{56}Co$ [41], which is one of the nuclei of interest early in collapse. However, this measurement has a 40% uncertainty. The sheer number of potentially important species, and their instability, makes direct measurements of all needed rates an impossibility. Nonetheless, measurements of neutrino-nucleus interactions remain extremely valuable by providing the most relevant constraints on the theoretical models. The proposed technique can be used in a very cost effective manner to measure the electron-neutrino capture cross section on any of a wide range of nuclei, wherein the natural abundance is dominated by a single isotope and the element is a solid at room temperature. Several such nuclei are in the critical nuclear mass range: ^{55}Mn, ^{59}Co, ^{89}Y, ^{93}Nb, ^{103}Rh and ^{115}In. Priority among these choices should be decided by their ability to constrain the theoretical rate calculations.

In addition to their effects prior to the formation of the supernova shock, charged current neutrino capture (and neutral current inelastic neutrino scattering [42]) on heavy nuclei above the shock can alter the entropy and neutronization of this infalling matter prior to its arrival at the shock. It has been suggested that if sufficient energy is transferred to this matter to melt a fraction of the nuclei, then the shock dynamics can be altered. Though this "pre-heating" of the shock (a misnomer as the material has a large specific heat on account of the heavy nuclei) could help the shock, it could also hinder the shock because the melted nuclei produce a higher pressure, reducing the Mach number of the shock. Potentially, these changes in the pre-shock matter affect not only the shock propagation but also the thermodynamic conditions in the post-shock convective region. **Only with accurate neutrino-nucleus cross sections can we gauge the full impact of these interactions on the supernova mechanism.**

3 Supernova Nucleosynthesis

Supernova nucleosynthesis is commonly divided into several "processes", each of which is impacted by neutrino-nucleus interactions. (1) Explosive nucleosynthesis occurs as a result of compressional heating by the supernova shock wave as it passes through the stellar layers. In the inner layers of the ejecta, where iron group nuclei result from α-rich freezeout, interactions with neutrinos alter the neutronization, changing the ultimate composition. (2) Neutrino nucleosynthesis or the "ν" process occurs due to neutrino-induced nuclear transmutations in the outer stellar layers followed by shock heating. (3) The rapid neutron capture or "r" process may occur in the neutrino-driven wind that emanates from the proto-neutron star after the explosion is initiated. **The neutrinos both drive the wind and interact with the nuclei in it. Early phases of this wind have also been suggested as the source of light p-process nuclei [43]. Thus, neutrino-nucleus interactions are important to all core collapse supernova nucleosynthesis processes.**

.

3.1 Neutrinos and the α-Rich Freezeout

One common property exhibited by recent spherically symmetric Boltzmann simulations [12,13] is a decrease in the neutronization (which is equivalent to an increase in Y_e) of the inner layers of the ejecta due to neutrino interactions. This is a feature that current parameterized nucleosynthesis models can not replicate because they ignore the neutrino interactions. The neutronization of the ejecta is important because galactic chemical evolution calculations and the relative neutron-poverty of terrestrial iron and neighboring elements strongly limits the amount of neutronized material that may be ejected into the interstellar medium by core collapse supernovae [44]. Those previous multidimensional models for core collapse supernovae that did produce explosions tended to greatly exceed these limits (see, e.g., [4,21,45]). To compensate, modelers have been forced to posit the fallback of a considerable amount of matter onto the neutron star, occurring on a timescale longer than was simulated. While the decreased neutronization seen in Boltzmann models reduces the need to invoke fallback, it also makes any fallback scenario more complicated, since the most neutron-rich material may no longer be the innermost.

As a result of neutrino-nucleus interactions, the nucleosynthesis products from future explosion simulations (utilizing Boltzmann neutrino transport) will be qualitatively different, both in composition and spatial distribution, from either parameterized bomb [46] or piston [30] nucleosynthesis models or the present generation of models of the core collapse mechanism. This is demonstrated in exploratory calculations by Hauser et al. [47] and Umeda et al. [48]. In the innermost ejecta, the shock fully dissociates the matter, so neutrino interactions with free nucleons dominate, producing a marked increase in the electron fraction. In more distant regions, cooler peak temperatures will cause more poorly known ν and $e^{\pm}$ interactions with heavy nuclei to dominate. These interactions, as well as neutral current inelastic neutrino scattering off these nuclei [42], are also important to the thermal balance, affecting the α-richness of the ejecta and, thereby, the abundance of important nuclei like ^{44}Ti, ^{57}Fe, ^{58}Ni and ^{60}Zn [30]. **Thus, there is a clear need for improved neutrino nucleus interaction rates in order to accurately calculate the iron-peak nucleosynthesis from core collapse supernovae.** Because the degree of neutronization is much less than in deeper layers of the star, several nuclei of interest are directly accessible via the proposed technique: ^{40}Ca, ^{45}Sc, ^{51}V, ^{55}Mn, ^{59}Co. However, theoretical calculations will still be necessary to provide full coverage of the many species present in significant concentrations.

3.2 Neutrino Nucleosynthesis

Neutrino nucleosynthesis is driven by the spallation of protons, neutrons, and alpha particles from nuclei in the overlying stellar layers by the intense neutrino flux that

is emanating from the central proto-neutron star powering the supernova [49]. Moreover, neutrino nucleosynthesis continues after the initial inelastic scattering reactions and the formation of their spallation products. The neutrons, protons, and alpha particles released continue the nucleosynthesis through further reactions with other abundant nuclei in the high-temperature supernova environment, generating new rare species. Neutrino nucleosynthesis occurs in two stages: (1) through neutrino irradiation and nuclear reactions prior to shock arrival and (2) through the continuation of nuclear reactions induced by neutrinos as the stellar layers expand and cool. The suggestion has been made [49] that neutrino nucleosynthesis is responsible for the production of ^{11}B, ^{19}F, as well as two of Nature's rarest isotopes: ^{138}La and ^{180}Ta.

Observations of the abundance of boron vary linearly with metallicity, implying that primary mechanisms that operate early in the history of our galaxy produce as much of these isotopes as secondary (quadratic) mechanisms that operate after the Galaxy has been enriched with metals. The competing mechanism for boron formation, cosmic ray spallation, is a secondary process. According to current models, neutrino nucleosynthesis in supernovae, which is a primary process, favors the production of ^{11}B over ^{10}B. However laboratory calibration of the spallation channels producing these two isotopes is needed. Used in conjunction with future HST observations discriminating between ^{10}B and ^{11}B, this measurement would be invaluable in resolving this controversy and supporting (or refuting) the suggestion that neutrino nucleosynthesis in supernovae is an important source of ^{11}B in the Galaxy [50]. ^{11}B and ^{10}B are produced through the following spallation channels:

$$^{12}\mathrm{C}(\nu,\nu' p)^{11}\mathrm{B}$$
$$^{12}\mathrm{C}(\nu,\nu' n)^{11}\mathrm{C}(e^{+}\nu)^{11}\mathrm{B}$$
$$^{12}\mathrm{C}(\nu,\nu' d)^{10}\mathrm{B}$$
$$^{12}\mathrm{C}(\nu,\nu' pn)^{10}\mathrm{B}.$$

It has been suggested [51] that the final abundance of ^{19}F produced in a supernova can serve as a "supernova thermometer" because the ratio of [^{19}F/^{20}Ne]/[^{19}F/^{20}Ne] (the denominator is the measured ratio in the Sun) is a measure of the mu and tau neutrinosphere temperatures (provided the abundance of ^{19}F produced in the supernova is due to neutrino nucleosynthesis). ^{19}F is produced through the following spallation channels:

$$^{20}\mathrm{Ne}(\nu,\nu' n)^{19}\mathrm{Ne}(e^{+}\nu_{e})^{19}\mathrm{F}$$
$$^{20}\mathrm{Ne}(\nu,\nu' p)^{19}\mathrm{F}.$$

Recent models [52], using improved neutrino nucleus reaction rates, show marked decreases in the production of ^{19}F.

That the rare isotopes ^{138}La and ^{180}Ta can be produced via neutrino nucleosynthesis in supernovae is compelling, and may serve as a very important

fingerprint of the neutrino process. If so, they potentially provide powerful diagnostics of the physics of the outer layers of the supernova. ^{138}La and ^{180}Ta are produced through the following charged and neutral current channels:

$$^{138}\mathrm{Ba}(\nu_e,e^-)^{138}\mathrm{La}$$
$$^{139}\mathrm{La}(\nu,\nu' n)^{138}\mathrm{La}$$
$$^{180}\mathrm{Hf}(\nu_e,e^-)^{180}\mathrm{Ta}$$
$$^{181}\mathrm{Ta}(\nu,\nu' n)^{180}\mathrm{Ta}.$$

Recent models [52] imply significantly larger production of these isotopes (with charged current (ν_e,e^-) reactions dominating for ^{138}La) enhancing the possibility that these isotopes originate in supernovae.

Experiments to directly measure the cross sections for all of these reactions are worthy of consideration, as are experiments which will better constrain the theoretical rates used in models thus far.

3.3 Nucleosynthesis in the Neutrino-Driven Wind

The astrophysical r-process (rapid neutron capture process) is responsible for roughly half of the Solar System's supply of elements heavier than iron. While the nuclear conditions necessary to produce the r-process are well established (see, e.g., [53]), the astrophysical site remains uncertain. The leading candidate is the neutrino-driven wind emanating from the proto-neutron star after a core collapse supernova is initiated [54]. Other plausible sites have been suggested [55,56], however all should result in neutrino-rich outflows. As the ejecta expands rapidly and cools, the nuclear composition is dominated by α-particles and free neutrons with a small concentration of iron group nuclei. As temperatures continue to drop, charged particle reactions "freeze out" while neutron capture reactions continue on the "seed" heavy nuclei present at freeze-out. Neutron capture (n,γ) reactions are balanced by their inverse photodisintegration (γ,n) reactions, establishing an equilibrium between the free neutrons and the nuclei in the wind. Because of the high concentration of free nucleons, this (n,γ)-(γ,n) equilibrium among isotopes of the same element produces nuclei that are quite neutron rich. β decays of nuclei with half lives that are short compared to the time scale for the r-process link these (n,γ)-(γ,n) clusters, producing nuclei with higher Z and leading to the synthesis of heavier elements [57].

Qian et al. [58] have demonstrated that neutrino-induced reactions can significantly alter the r-process path and its yields in both the (n,γ)$\leftrightarrow$(γ,n) equilibrium phase and the "postprocessing phase" that occurs once these reactions fall out of equilibrium. In the presence of a strong neutrino flux, ν_e-induced charged current reactions on the waiting point nuclei at the magic neutron numbers N=50,82,126 might compete with beta decays and speed up passage through these bottlenecks. Also, neutrinos can inelastically scatter on r-process nuclei via ν_e-induced charged-current

reactions and ν-induced neutral-current reactions, leaving the nuclei in excited states that subsequently decay via the emission of one or more neutrons. This processing may for example shift the abundance peak at A=195 to smaller mass. Extending this, Haxton et al. [59] pointed out that neutrino postprocessing effects would provide a fingerprint of a supernova r-process. Eight abundances are particularly sensitive to the neutrino postprocessing: ^{124}Sn, ^{125}Te, ^{126}Te, ^{183}W, ^{184}W, ^{185}Re, ^{186}W, and ^{187}Re. Observed abundances of these elements are consistent with the postprocessing of an r-process abundance pattern in a neutrino fluence consistent with current supernova models. If the neutrino interaction leaves the daughter in a sufficiently excited state, fission may result [60,61], potentially linking the mass 195 peak to the mass 130 peak. Some such correlation is suggested by observations of ultra-metal poor stars (see, e.g., [62]).

On a more pessimistic note, Meyer, McLaughlin, and Fuller [63] have investigated the impact of neutrino-nucleus interactions on the r-process yields and have discovered that electron neutrino capture on free neutrons and heavy nuclei (in the presence of a strong enough neutrino flux) can actually hinder the r-process by driving the neutrino-driven wind proton rich, posing a severe challenge to theoretical models. However, this push to lower neutronization makes the early phases of the neutrino-driven wind a candidate for production of the light p-process nuclei like ^{74}Se, ^{78}Kr, ^{84}Sr and ^{92}Mo [43]. The abundances of these species are likely highly sensitive to neutrino-nucleon interactions. Simulations by Meyer [64] showed that significant amounts of ^{92,94}Mo are only produced when neutrino-nucleus interactions are included, with neutrino-nucleus interactions on nuclei with $Z \geq 40$ (particular ^{92}Zr) most responsible for the enhancement of the production of ^{92,94}Mo.

While the neutrino-nucleus reactions of direct interest for the p-process nuclei are accessible, during the r-process and subsequent postprocessing in the supernova neutrino fluence, neutrinos interact with extremely neutron-rich, radioactive nuclei. Thus, relevant direct neutrino-nucleus measurements cannot be made. However, indirect measurements of charged- and neutral-current neutrino-nucleus interactions on heavy stable nuclei for A>80 would be invaluable as a gauge of the accuracy of theoretical predictions.

4 Supernova Neutrino Detection

The twenty neutrino events detected by IMB and Kamiokande from SN1987A confirmed a central tenant of supernova theory—that core collapse supernovae mark the formation of a proto-neutron star and release of the liberated binding energy in the form of neutrinos—and signaled the birth of extra-Solar-System neutrino astronomy. For a Galactic supernova, thousands of events will be seen by SuperKamiokande [69] and SNO[70], which for the first time will give us detailed neutrino "light curves" and bring us volumes of information about the deepest regions in the explosion. In turn, these light curves can be used to test and improve supernova models, thereby improving predictions about the explosion and resultant nucleosynthesis. Moreover, from these detailed neutrino light curves and an understanding of the effects of neutrino oscillations, interesting insight could be gained about the density structure of the supernova progenitor. Recently, Beacom and Vagins [71] suggested a modification of Super-

Kamiokande that would allow detection of the diffuse supernova neutrino background, i.e., the flux from all supernovae in the universe, at the rate of 2-6 events per year. In just a few years, the yield from SN 1987A could be exceeded, allowing improved tests of numerical supernova models through the measured flux and spectral shape. In addition, this should also allow pre-supernova neutrino observations of massive stars within 1 kpc [72]. Among the neutrino-nucleus interactions of relevance for supernova neutrino detection are neutrino interactions on ^{2}H, ^{16}O, ^{56}Fe and ^{206,207,208}Pb.

4.1 Deuterium

Neutrino experiments that use heavy water, like the Sudbury Neutrino Observatory (SNO), can detect supernova neutrinos via four main channels:

$$e^{-}(\nu,\nu')e^{-}$$
$$d(\nu,\nu n)p$$
$$d(\nu_e,e^{-}p)p$$
$$d(\bar{\nu}_e,e^{+}n)n$$

Measurement of the reaction $d(\nu_e,e^{-}p)p$, which has been suggested as a calibration for the reaction $p(p,e^{+}\nu_e)d$ (part of the pp chain of reactions powering the Sun), would also provide a calibration for heavy water neutrino detectors. Monte Carlo studies suggest that for the source brightness predicted for the ORNL SNS, two years of data in approximately thirty fiducial tons of D_2O would yield a cross section measurement with an accuracy of a few percent [73], which in turn will enable a more accurate interpretation of the SNO data from the next Galactic supernova. This measurement would also serve as an important test case for the effective field theory approach to neutrino-nucleus interactions (see [74] and references therein).

4.2 Oxygen

The charged-current reaction $^{16}O(\nu_e,e^{-})^{16}F$ is the principal channel for electron neutrino interactions for thermal sources in the range $T_{\nu_e}\geq$4-5 MeV, and its rate exceeds that of neutrino-electron scattering by an order of magnitude for $T_{\nu_e}\geq$7-9 MeV [75]. Moreover, the electron angular distribution is strongly correlated with the electron neutrino energy [76], providing a way to measure the incident neutrino energy and, consequently, the electron neutrino spectra.

In addition, the appearance of back-angle electron emission from this reaction in, for example, Super-K would result from energetic electron neutrinos, more energetic than predicted by supernova models, providing further evidence for flavor oscillations and thereby information about the mu and tau neutrino spectra emanating from supernovae [76]. Mu and tau neutrinos in the stellar core couple to the core material only via neutral currents, whereas electron neutrinos and antineutrinos couple via both neutral and charged currents. As a result, the former decouple at higher density and, therefore, temperature, and have harder spectra. Utilizing reactions on ^{16}O, Langanke, Vogel, and

Kolbe [77] have suggested a novel way of also unambiguously identifying mu and tau neutrino signatures in Super-K. The larger average energies for these neutrino flavors may be sufficient to excite giant resonances via the neutral-current reactions $^{16}O(\nu_{\mu,\tau},\nu'_{\mu,\tau})^{16}O^*$. These resonances are above particle threshold and subsequently decay via the emission of protons, neutrons, and gamma rays. The gamma rays would provide the mu and tau neutrino signatures. The two decay channels are: $^{16}O^*(,\gamma n)^{15}O$ and $^{16}O^*(,\gamma p)^{15}N$. However, potential channels for observing the mu and tau neutrinos from supernovae must be reexamined in light of recent work (see, e.g., [78,79,68]), which indicates that nucleon-nucleon bremsstrahlung and the effects of nuclear recoil in neutrino-nucleon scattering significantly soften the mu and tau neutrino spectra, lessening their energy excess over electron neutrinos (see Figure 3). **Thus, accurate measurements of both charged- and neutral-current neutrino cross sections on ^{16}O would serve as a foundation for interpreting the neutrino data from the next Galactic core collapse supernova and for using the data to potentially observe the ν_μ and ν_τ neutrino spectra as it is emitted from the proto-neutron star.** An experiment to measure the cross section for:

$$^{16}O(\nu_e,e^-)^{16}F$$

should be a high priority for a stopped pion facility. Further useful experiments could focus on the cross sections for:

$$^{16}O(\nu_\mu,\nu'_\mu n\gamma)^{15}O$$
$$^{16}O(\nu_\mu,\nu'_\mu p\gamma)^{15}N.$$

1.4.3 Iron and Lead

The use of iron and lead in supernova neutrino detectors like the proposed OMNIS detector would provide another way of detecting the mu and tau neutrino spectra in core collapse supernovae [80]. Iron has a sufficiently high threshold for neutron production via charged-current neutrino interactions that such production is negligible, whereas in lead neutrons are produced by both charged- and neutral-current interactions. Oscillations between the more energetic mu and tau neutrinos and the electron neutrinos would boost the charged-current event rate while leaving the neutral-current rate roughly unchanged. Thus, the ratio of the event rate in lead to that in iron would serve as a further constraint on the extent of neutrino oscillations and the emitted mu/tau spectra. However, this potential channel for observing the mu and tau neutrinos must also be reexamined in light of the softening of the mu and tau neutrino spectra.

To further the development of a detector like OMNIS, experiments to measure the neutrino-iron and neutrino-lead cross sections have been proposed. For iron, the neutral-current reaction:

$$^{56}Fe(\nu,\nu' n)^{55}Fe$$

dominates. For lead, a total cross section would be measured resulting from the following neutral- and charged-current channels:

$$^{208}\mathrm{Pb}(\nu,\nu' n)^{207}\mathrm{Pb}$$
$$^{208}\mathrm{Pb}(\nu,\nu' 2n)^{206}\mathrm{Pb}$$
$$^{208}\mathrm{Pb}(\nu_e,e^- n)^{207}\mathrm{Bi}$$

including also the channels for the isotopes ^{206}Pb and ^{207}Pb. For this reason, as well as their importance to nucleosynthesis, iron and lead cross section measurements should be among the first experiments at a stopped pion facility.

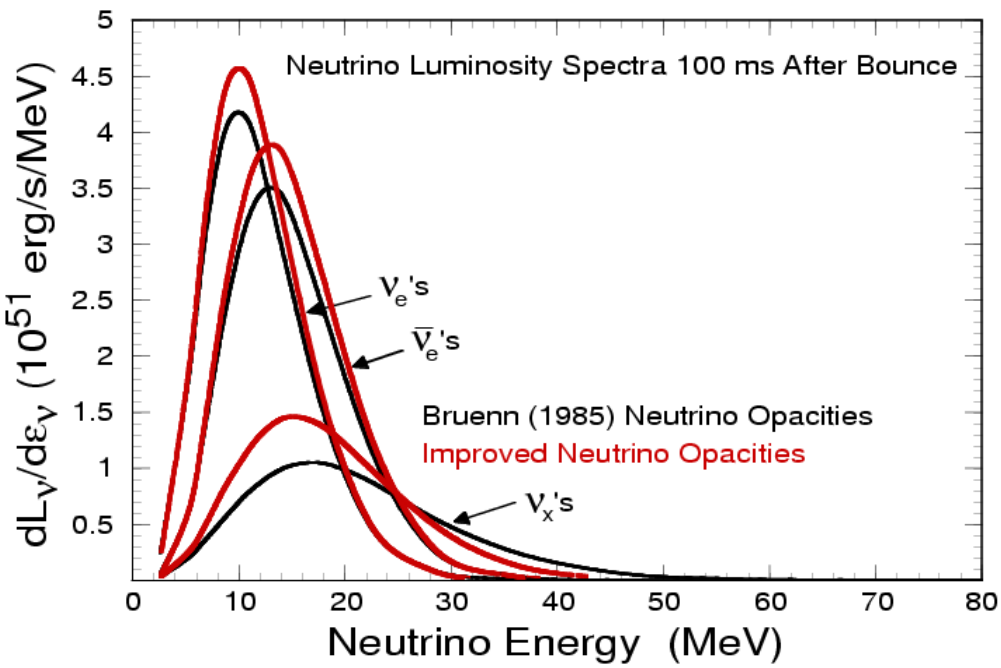

Figure 3: Comparison of the neutrino spectra from supernova simulations using the standard [7] opacities (black) and updated opacities (red; including the effects of neutino-nucleon absorption and elastic scattering [65], neutrino-nucleon inelastic scattering and bremsstrahlung [66], and weak magnetism [67]). The simulations, initiated from a 13 M progenitor, are fully general relativistic, and the spectra are computed at a radius of 500 km, 100 milliseconds after bounce [68].

5 Conclusion

With a neutrino source as intense as the ORNL Spallation Neutron Source, we are presented with a unique opportunity, given the overlap between the facility and supernova neutrino spectra, to provide an experimental foundation for the many neutrino-nucleus weak interaction rates needed in supernova models. This would enable more realistic supernova models and allow us to cull fundamental physics from these models

with greater confidence when their predictions are compared with detailed observations. Charged- and neutral-current neutrino interactions on nuclei in the stellar core play a central role in supernova dynamics and nucleosynthesis and are also important for supernova neutrino detection. Measurements of these reactions on select, judiciously chosen targets would provide an invaluable test of the complex theoretical models used to compute the neutrino-nucleus cross sections.

1) References

[1] Burrows A and Lattimer J. M 1985 *ApJ* **299** L19–L22.
[2] Wilson J. R 1985 Numerical Astrophysics (Boston) (ed Centrella J. M, LeBlanc J. M, and Bowers R. L) Jones and Bartlett pp 422–434.
[3] Bethe H. H and Wilson J. R 1985 *ApJ* **295** 14–23.
[4] Janka H.-T and Müller E 1996 *A&A* **306** 167.
[5] Burrows A and Goshy J 1993 *ApJ* **416** L75–L78.
[6] Arnett W. D 1977 *ApJ* **218** 815–833.
[7] Bruenn S. W 1985 *ApJS* **58** 771–841.
[8] Myra E. S, Bludman S. A, Hoffman Y, Lichenstadt I, Sack N, and van Riper K. A 1987 *ApJ* **318** 744–759.
[9] Wilson J. R and Mayle R. W 1993 *Phys. Rep.* **227** 97–111.
[10] Janka H.-T 1992 *A&A* **256** 452–458.
[11] Messer O. E. B, Mezzacappa A, Bruenn S. W, and Guidry M. W 1998 *ApJ* **507** 353.
[12] Rampp M and Janka H.-T 2000 *ApJ* **539** L33–L36.
[13] Mezzacappa A, Liebendörfer M, Messer O, Hix W, Thielemann F.-K, and Bruenn S 2001 *Phys. Rev. Lett.* **86** 1935.
[14] Liebendörfer M, Mezzacappa A, Thielemann F.-K, Messer O. E. B, Hix W. R, and Bruenn S. W 2001 *Phys. Rev. D* **63** 103004.
[15] Thompson T. A, Burrows A, and Pinto P. A 2003 *ApJ* **592** 434–456.
[16] Mezzacappa A, Calder A. C, Bruenn S. W, Blondin J. M, Guidry M. W, Strayer M. R, and Umar A. S 1998 *ApJ* **493** 848.
[17] Keil W, Janka H.-T, and Müller E 1996 *ApJ* **473** L111–L114.
[18] Buras R, Rampp M, Janka H.-T, and Kifonidis K 2003 *Phys. Rev.Lett.* **90** 241101.
[19] Bruenn S. W and Dineva T 1996 *ApJ* **458** L71–L74.
[20] Bruenn S, Raley E, and Mezzacappa A 2004 *ApJ* .
[21] Herant M, Benz W, Hix W. R, Fryer C. L, and Colgate S. A 1994 *ApJ* **435** 339–361.
[22] Burrows A, Hayes J, and Fryxell B. A 1995 *ApJ* **450** 830–850.
[23] Fryer C. L and Warren M. S 2002 *ApJ* **574** L65–LL68.
[24] Blondin J, Mezzacappa A, and DeMarino C 2003 *ApJ* **584** 971–980.
[25] Mezzacappa A, Calder A. C, Bruenn S. W, Blondin J. M, Guidry M. W, Strayer M. R, and Umar A. S 1998 *ApJ* **495** 911.
[26] Heger A, Langanke K, Martínez-Pinedo G, and Woosley S. E 2001 *Phys. Rev. Lett.* **86** 1678–1681.
[27] Liebendörfer M, Messer O. E. B, Mezzacappa A, and Hix W. R 2001 Proceedings of the 20th Texas Symposium on Relativistic Astrophysics (Melville) (ed Wheeler J and Martel H) AIP pp 472–477.
[28] Langanke K and Martínez-Pinedo G 2000 *Nucl. Phys. A* **673** 481–508.
[29] Oda T, Hino M, Muto K, Takahara M, and Sato K 1994 *Atomic Data and Nuclear Data Tables* **56** 231.
[30] Woosley S. E and Weaver T. A 1995 *ApJS* **101** 181.
[31] Fuller G. M, Fowler W. A, and Newman M. J 1985 *ApJ* **293** 1–16.
[32] Mazurek T. J 1973 Ph.D. thesis Yeshiva University.
[33] Hansen C. J 1966 Ph.D. thesis Yale University.
[34] Yahil A 1983 *ApJ* **265** 1047–1055.
[35] Langanke K, Martinez-Pinedo G, Sampaio J. M, Dean D. J, Hix W. R, Messer O. E. B, Mezzacappa A, Liebendoerfer M, Janka H.-T, and Rampp M 2003 *Phys. Rev. Lett.* **90**

241102.
[36] Hix W. R, Messer O. E. B, Mezzacappa A, Liebendoerfer M, Sampaio J. M, Langanke K, Martinez-Pinedo G, and Dean D. J 2003 *Phys.Rev. Lett.* 201102.
[37] Hix W. R 1995 Ph.D. thesis HARVARD UNIVERSITY.
[38] Bravo E and García-Senz D 1999 *MNRAS* **307** 984–992.
[39] El Eid M. F and Hillebrandt W 1980 *A&AS* **42** 215–226.
[40] Brachwitz F, Dean D, Hix W, Iwamoto K, Langanke K, Martinez-Pinedo G, Nomoto K, Strayer M. R, and Thielemann F.-K 2000 *ApJ* **536** 934–947.
[41] Maschuw R 1998 *Prog. Part. Phys.* **40** 183.
[42] Bruenn S. W and Haxton W. C 1991 *ApJ* **376** 678–700.
[43] Hoffman R. D, Woosley S. E, Fuller G. M, and Meyer B. S 1996 *ApJ* **460** 478.
[44] Trimble V 1991 *A&AR* **3** 1–46.
[45] Kifonidis K, Plewa T, Janka H.-T, and Müller E 2000 *ApJ* **531** L123–L126.
[46] Thielemann F.-K, Nomoto K, and Hashimoto M 1996 *ApJ* **460** 408.
[47] Hauser P, Martinez-Pinedo G, Hix W, Liebendšrfer M, Mezzacappa A, and Thielemann F.-K 2004 *ApJ* in preparation.
[48] Umeda H, Nomoto K, Hix W, Thielemann F.-K, and Liebendšrfer M 2004 *ApJ* in preparation.
[49] Woosley S. E, Hartmann D. H, Hoffman R. D, and Haxton W. C 1990 *ApJ* **356** 272–301.
[50] Hartmann D, Myers J, Woosley S, Hoffman R, and Haxton W 1999 ASP Conf. Ser. 171: LiBeB Cosmic Rays, and Related X- and Gamma-Rays p 235.
[51] Haxton W 1999 NEUTRINOS IN PHYSICS AND ASTROPHYSICS From 10^{-33} to 10^{28} cm (TASI 98) (Singapore) (ed Langacker P) World Scientific pp 432–487.
[52] Heger A, Kolbe E, Haxton W, Langanke K, Martinez-Pinedo G, and Woosley S 2003 *Phys. Rev. Lett.* submitted.
[53] Kratz K.-L, Bitouzet J.-P, Thielemann F.-K, Möller P, and Pfeiffer B 1993 *ApJ* **403** 216–238.
[54] Woosley S. E, Wilson J. R, Mathews G. J, Hoffman R. D, and Meyer B. S 1994 *ApJ* **433** 229–246.
[55] Wheeler J. C, Cowan J. J, and Hillebrandt W 1998 *ApJ* **493** L101–L104.
[56] Freiburghaus C, Rosswog S, and Thielemann F.-K 1999 *ApJ* **525** L121–L124.
[57] Meyer B. S 1994 *ARA&A* **32** 153–190.
[58] Qian Y.-Z, Haxton W. C, Langanke K, and Vogel P 1997 *Phys.Rev. C* **55** 1532–1544.
[59] Haxton W. C, Langanke K, Qian Y.-Z, and Vogel P 1997 *Phys.Rev. Lett.* **78** 2694–2697.
[60] Qian Y.-Z 2002 *ApJ* **569** L103–L106.
[61] Kolbe E, Langanke K, and Fuller G. M 2003 *preprint* astro-ph/0308350.
[62] Sneden C, Cowan J. J, Lawler J. E, Ivans I. I, Burles S, Beers T. C, Primas F, Hill V, Truran J. W, Fuller G. M, Pfeiffer B, and Kratz K 2003 *ApJ* **591** 936–953.
[63] Meyer B. S, McLaughlin G. C, and Fuller G. M 1998 *Phys. Rev. C* **58** 3696–3710.
[64] Meyer B. S 2003 *Nucl. Phys. A* **719** 13–20.
[65] Reddy S, Prakash M, and Lattimer J. M 1998 *Phys. Rev. D* **58** 013009.
[66] Hannestad S and Raffelt G 1998 *ApJ* **507** 339–352.
[67] Horowitz C. J 2002 *Phys. Rev. D* **65** 43001.
[68] Bruenn S. W 2004 *ApJ* in preparation.
[69] Beacom J. F and Vogel P 1998 *Phys. Rev. D* **58** 053010.
[70] 1998 *Phys. Rev. D* **58** 093012.

[71] Beacom J. F and Vagins M. R 2004 *Phys. Rev. Lett.* submitted;hep-ph/0309300.
[72] Odrzywolek A, Misiaszek M, and Kutschera M 2004 *Astroparticle Physics* submitted; astro-ph/0311012.
[73] Avignone F. T and Efremenko Y. V 2003 *Journal of Physics G Nuclear Physics* **29** 2615–2628.
[74] Gudkov V and Kubodera K 2003 *Journal of Physics G Nuclear Physics* **29** 2597–2613.
[75] Haxton W. C 1987 *Phys. Rev. D* **36** 2283–2292.
[76] Kolbe E, Langanke K, Martínez-Pinedo G, and Vogel P 2003 *Journal of Physics G Nuclear Physics* **29** 2569–2596.
[77] Langanke K, Vogel P, and Kolbe E 1996 *Phys. Rev. Lett.* **76** 2629–2632.
[78] Thompson T. A, Burrows A, and Horvath J. E 2000 *Phys. Rev. C* **62** 035802.
[79] Raffelt G. G 2001 *ApJ* **561** 890–914.
[80] Boyd R. N, Murphy A. S, and OMNIS collaboration 2001 *Nucl.Phys. A* **688** 386–389.

Appendix-III.

Nuclear Science

Nuclei are correlated quantum-many body systems that can be excited by neutrinos through a variety of channels. For example neutrinos with energies less than 15 MeV excite nuclei mainly through the Gamow-Teller resonance, while higher energy neutrinos will also excite first and second forbidden transitions within the nucleus. ν-SNS will enable studies of nuclear excitations that would be difficult to generate or analyse with any other kind of experiment. Using experimental information obtained from the ν-SNS would allow for a calibration of nuclear structure calculations of neutrino cross sections.

The motivation for constraining nuclear structure theory comes from the needs of astrophysics (discussed in the astrophysics appendix). To reiterate, during the collapse of a dying star, many neutron-rich isotopes between mass 50 and 100 are formed and destroyed via electron and neutrino capture, and we would like to know all the corresponding cross sections. Later on, after the core bounce, neutrinos create many new isotopes from existing ones by knocking out neutrons; we would also like to understand the rates at which this ``neutrino-process'' synthesizes elements. We cannot measure all the reactions. In fact, we sometimes can't even measure cross sections on the targets we will have -- prospective supernova detectors, for example -- at the energies we would like. So how much will rates we can measure help us determine all those we cannot? The short answer is that while ν-SNS reactions by themselves cannot fill in all the unknown physics in our calculations, they can provide unique and sometimes nearly sufficient information. When the information is less complete, experiments with monoenergetic beams of other particles --- protons or light nuclei in charge-exchange reactions and electrons or protons in neutral current reactions -- can complement it. The data won't ever quite allow a model-independent determination of what we want, but will severely constrain the nuclear-structure theory on which we must rely.

There are three reasons why the constraints will be strong. First, in some cases the reactions we care about have incoming neutrino spectra quite close to those at ν-SNS, so that provided we can identify the necessary outgoing particles the ν-SNS measurement alone will almost tell us what we want to know. Second, the neutrino reactions at N-SNS energies and below proceed largely through a few multipoles of the weak interaction with spin J<=3. Thus a limited number of nuclear operators determine the cross sections, and some information about their matrix elements can be extracted from other kinds of experiments in which kinematics are better controlled. Finally, the strength in the few important multipoles is often concentrated in collective nuclear resonances, which usually have relatively simple structure, are subject to sum rules, and can be modeled effectively through, e.g., the random phase approximation or the shell model. The important resonances in neutrino-electron reactions are the allowed $J^{\pi}=1^{+}$ Gamow-Teller (GT) mode, and the forbidden 1^{-} dipole and 0^{-} -- 1^{-} -- 2^{-} spin-dipole (SD) modes. In neutral current reactions, the analogs of these resonances are the most important.

We now relate through a few examples the extent to which ν-SNS can be used to constrain nuclear theory. The first example is related to supernova astrophysics since many of the cross sections that are of astrophysical interest require one to understand the interactions of neutrinos on unstable nuclei. Direct measurements on unstable nuclei will not be possible with the ν-SNS facility nor with any envisioned neutrino-nucleus facility. However, the measurements that are made by ν-SNS will be very useful to constrain nuclear models that are employed to predict neutrino cross sections on unstable nuclei. We demonstrate this important point in the N-Z chart of nuclei. With just seven of the 36 affordable nuclear targets, we obtain the ability to calibrate nuclear theory calculations for neutrino cross sections throughout the periodic table and particularly in the regions of interest to supernova science. Superimposed on the figure are circles of radius 8 nucleons centered on the nuclear target. Reliable extrapolations from experimental data could be made in within these circles up to lines where major shell closures are crossed. If we were to plot all 36 circles, we would see complete coverage of the entire nuclear chart through Pb. Thus, for the supernova explosion, and for neutrino nucleosynthesis, ν-SNS will make definitive measurements that, when combined with reliable nuclear theory, will give us a reasonable picture of neutrino cross sections on unstable nuclei. The selected target materials for this plot are: ^{40}Ca, ^{56}Fe, ^{75}As, ^{89}Y, ^{127}I, ^{165}Ho, and ^{208}Pb.

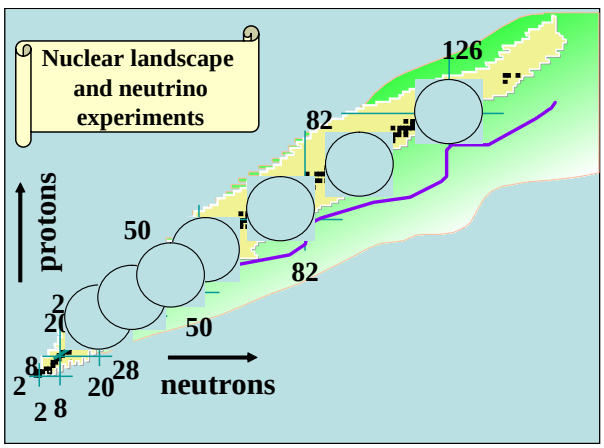

If the nuclear theory that produces known experimental data (nuclear structure information such as masses, decay half-lives, low-lying spectra, and giant-resonance states) on unstable systems is taken as reliable, and if it also reproduces neutrino-nucleus cross-section measurements on stable nuclei, then we will have a reasonable estimate of neutrino-nucleus cross sections for unstable systems. For lighter systems (through mass 65) various shell-model approaches could be employed, while for heavier systems modern mean-field theories combined with RPA could be used to describe the cross sections. We note that for unstable nuclei a number of new approaches are being developed today (ranging from mean-field theories to shell models that include continuum effects) that could also be utilized to calculate cross section information. Most of these developments are targeted at understanding masses, beta-decay, and spectroscopy of nuclear systems. The experiments at ν-SNS could obviously be used to validate our theoretical understanding of higher-energy nuclear excitations within the same models.

We discuss another example of the impact that ν-SNS will have on nuclear theory and the relationship of nuclear theory and astrophysics in these problems. Again, the important point is that ν-SNS can be used to calibrate nuclear theory. This example comes from supernova explosion detection. Unless the MSW mechanism is operating in

supernovae, the electron neutrinos from an explosion (detected through charge-exchange reactions) will mostly have energies on the order of 10 MeV, not enough to strongly excite the forbidden spin-dipole resonances. Then existing (p,n) measurements in 54Fe and 208Pb, from which the GT strength distributions can be extracted, nearly determine the cross section. On the other hand, if MSW oscillations do occur, some of the electron neutrinos will have energies on the order of 25 MeV. Now allowed transitions will contribute only about half of the cross section, the other half coming from the dipole and spin-dipole resonances. Although (p,n) experiments have identified these resonances in lead, they could not completely untangle the various multipoles, making it impossible to extract the nuclear matrix elements necessary to compute neutrino cross sections. While these data may improve in the future, and are important checks on any calculation of neutrino cross sections, at these energies the most important check by far will come from the ν-SNS cross section itself, which is exactly what we want save for a slight difference in the spectrum of incoming neutrinos.

A third area in which ν-SNS measurements will make a contribution involves the possibility to study interesting nuclear structure issues related to the weak interaction. We need to understand the ratio of the axial to vector coupling constants. For the Gamow-Teller operator that arises from the low-energy expansion of the weak interaction, one finds that this ratio is modified by the nuclear medium. It is unknown whether other operators in the weak interaction are similarly modified. Using the SNS to probe medium energy distributions of strength in ν-A scattering (by binning the cross section with respect to the outgoing electron energy) would open the possibility to investigate this fundamental problem. This measurement could be performed on any target material for which low-energy pn-reaction experiments are available in order to compare low-energy excitations. These excitations can be obtained within the shell-model. Furthermore, a judicious choice of SNS neutrino targets that can simultaneously be developed for inelastic electron scattering at the GSI facility in Darmstadt, could yield simultaneous information on both neutral current (via indirect measurements at GSI-Darmstadt) and charged current (at the SNS) neutrino scattering in similar energy windows. This complementary information could be used to evaluate nuclear models that have been developed to predict total neutrino scattering cross sections.

Appendix – IV

Homogeneous Detector

The homogeneous detector consists of a 3.5 m × 3.5 m × 3.5 m steel vessel with 600 8″ photomultiplier tubes (PMTs) mounted uniformly on the inner walls, to provide approximately 38% photocathode coverage. A schematic drawing of the detector is shown in Fig. 1 below. The actual distribution and orientation of the PMTs will be optimized using Monte Carlo simulations. For instance, it is expected that the edge and corner PMTs should be angled such that the light collection efficiency is maximized. The 38% surface coverage should allow the detector to have a very good event reconstruction and particle identification when operating with a variety of fluids as active media (such as mineral oil, water, heavy water, etc.), regardless of the amount of scintillator doping (i.e., operating just as a pure Čerenkov imaging detector).

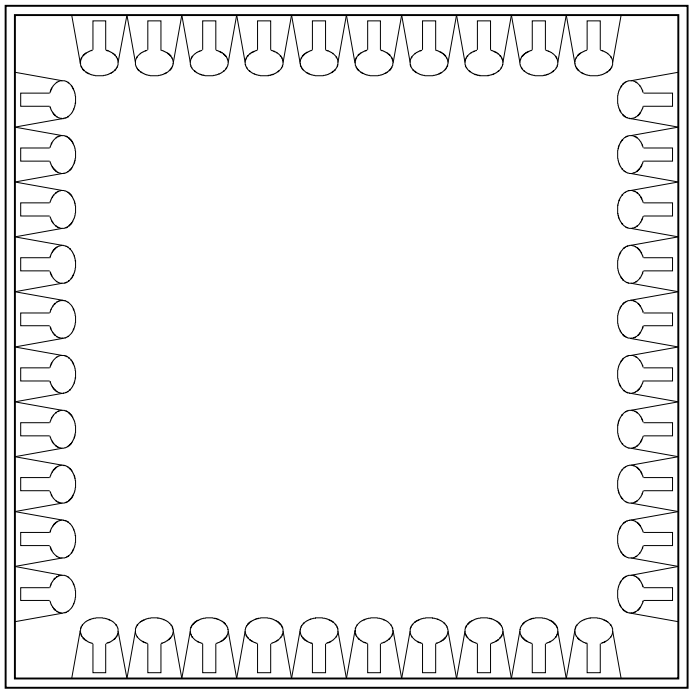

Figure 1: Schematic view of the ν–SNS homogeneous detector (to scale).

A good candidate for the PMTs to be used in this detector is the Hamamatsu R5912, which is currently successfully used in the MiniBooNE experiment at Fermilab. This PMT has a reasonably good single photoelectron (PE) charge and time response ($\sigma_t = 1.2$ ns), as we illustrate in Fig. 2 below. These distributions have been obtained from the low-intensity laser calibration data in MiniBooNE.

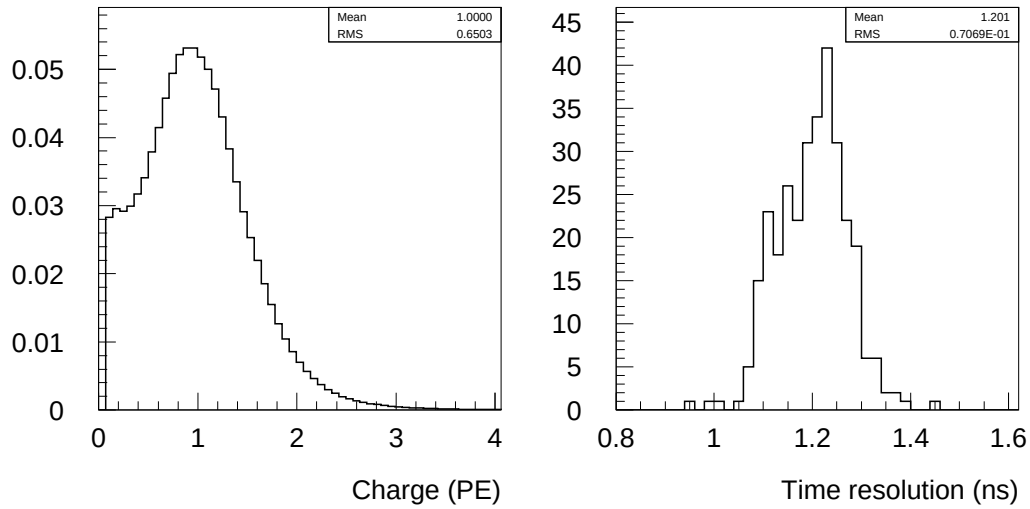

Figure 2: Single PE charge response (left) and time resolution distribution (right) for the 340 MiniBooNE Hamamatsu R5912 PMTs.

The *in situ* calibration of the PMTs (gains, time offsets and slewing) will be performed using a system similar to that used in MiniBooNE and its precursor, the Liquid Scintillator Neutrino Detector (LSND). It consists of an external laser of tunable wavelength which delivers short light pulses through an optical fiber to a flask inside the tank, which scatters the light isotropically. In contrast to LSND and MiniBooNE which used 3 and 4 flasks, respectively, at fixed positions in the detector, we would use here a single flask, which can be moved in a controlled manner throughout the active region of the tank. The energy calibration of the detector can be easily performed using large samples of Michel electrons from the decays of stopped cosmic-ray muons, with an endpoint energy of 52.8 MeV. In addition, it is possible to deploy radioactive sources in the tank for calibration at lower energies, and also for testing the accuracy of the reconstruction algorithms.

The data acquisition (DAQ) for the homogeneous detector can also be based on the robust and well-tested design used in LSND and MiniBooNE, which runs at 10 MHz. While this is too slow to record the PMT anode pulses directly, a "QT board" converts these pulses into more slowly varying signals which still contain the necessary charge and time information. The anode signal feeds an integrating capacitor with a time constant of approximately $\tau = 1200$ ns. The voltage V_q across the capacitor is digitized every 100 ns, in step with the 10 MHz clock. If the pulse is large enough to fire the on-board discriminator (set typically to about 0.25 PE), a separate voltage V_t begins ramping linearly away from the baseline. The ramp continues until two clock ticks have passed, at which point it is rapidly reset to the baseline. V_t is also digitized every 100 ns. The DAQ software looks continuously at the stream of digitized V_q and V_t

numbers coming from each channel and, if the discriminator has fired, it records a set of four V_q and V_t values: one before the discriminator fired and three after. This process is illustrated schematically in Fig. 3. The actual charge and time reconstruction of the hit is performed at a higher level in the software, using the recorded V_q and V_t "quads". Alternatively, one can consider a more sophisticated DAQ system, which performs a full digitization of the anode pulses – similar to that used in the KamLAND experiment.

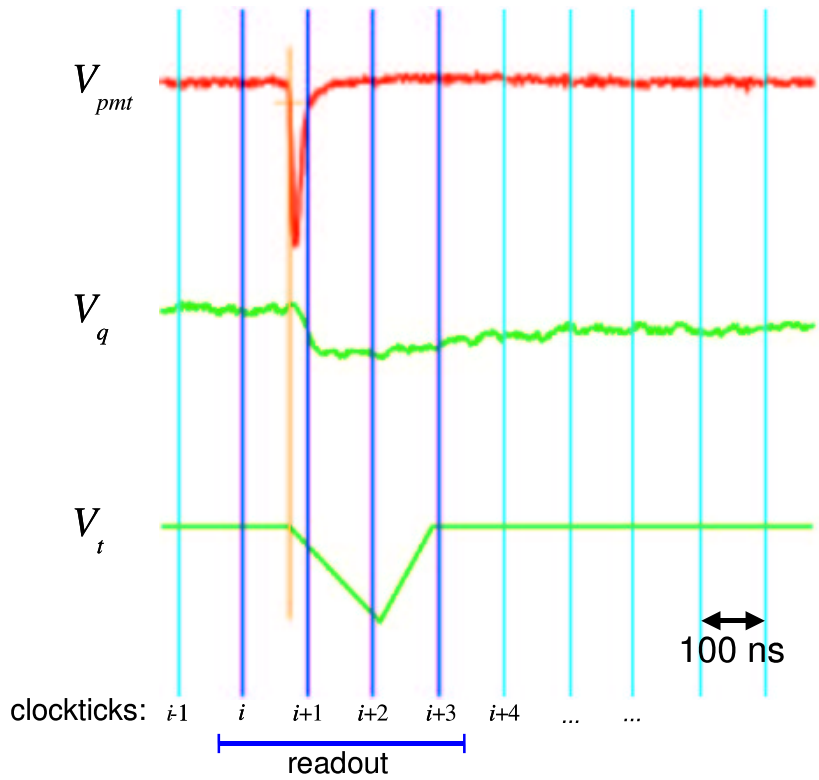

Figure 3: Pulses in the front-end electronics: V_{pmt} is the incoming anode signal and V_q is its integral, convoluted with and exponential decay. The vertical orange line indicates the firing of the discriminator which starts the time ramp V_t and is reset after two clock ticks. For this hit the DAQ records the four V_q and V_t values digitized at i, $i+1$, $i+2$, and $i+3$.

Considering the extremely low duty factor of the SNS beam, the DAQ system can be triggered simply by a precursor signal from the accelerator. The circular buffers will be large enough to hold and write all detector data in a time window of about 20 μs (or longer) around the 0.7 μs beam spill. This time window will record a large enough amount of beam off data, necessary for both detector studies and also for the beam on/off subtraction. In addition, special purpose triggers will be used for control data sample recording (such as laser calibration, Michel electrons, etc.)

From our experience with the LSND and MiniBooNE detectors and the configuration of this apparatus, we expect an energy resolution of approximately 5–7% at 53 MeV (depending on the amount of light per MeV collected for each particular active medium), a spatial position resolution of about 15–20 cm, and an angular resolution of approximately 3–5°. The event reconstruction and particle identification can also be largely based on the powerful maximum likelihood techniques developed for the final LSND analyses and MiniBooNE. All of the parameters necessary for these techniques (such as charge and time likelihoods, attenuation lengths, PMT quantum efficiencies, etc.) can be determined directly from the large amounts of control data samples recorded during the beam off periods, such as Michel electrons from stopped cosmic-ray muon decays, cosmic-ray neutrons, etc. These samples will provide invaluable checks of the reconstruction and particle identification performance and efficiencies, in a manner largely independent of the Monte Carlo simulations.

Assuming an average neutrino flux $\Phi = 10^7\,\mathrm{s}^{-1}\,\mathrm{cm}^{-2}$ for each neutrino flavour at the detector location, the event rate for mineral oil – which is mostly C_nH_{2n+2}, with $n \approx 20$ – yields 90 events $\mathrm{yr}^{-1}\,\mathrm{m}^{-3}$ for the charged-current $\nu_e C$ reaction alone. Here we have used $\sigma = 9.1 \times 10^{-42}\,\mathrm{cm}^{-2}$ for the transition to the ground state, $\nu_e C \to e^- N_{gs}$, and $\sigma = 5.9 \times 10^{-42}\,\mathrm{cm}^{-2}$ for the transition to the excited states, $\nu_e C \to e^- N^*$, where both cross sections have been averaged over the incident ν_e decay-at-rest energy spectrum. The mineral oil density has been taken to be $\rho = 0.85\,\mathrm{g/cm}^3$, which yields a total number of 3.66×10^{28} carbon atoms per cubic meter of mineral oil. The event rate quoted above contains no corrections for the electron detection and identification efficiencies, and assumes that the accelerator runs 200 days per year with a 95% live-time. The volume defined by the surface of the PMTs represents $24.4\,\mathrm{m}^3$ from the total volume of $42.9\,\mathrm{m}^3$. Assuming a fiducial volume that extends to only 20 cm from the PMT faces, this yields $15.5\,\mathrm{m}^3$, which in turn implies $1,400$ $\nu_e C$ events per year – before any detection and reconstruction efficiencies are applied. We expect that an efficiency of 60–70% can be easily achieved with such a detector in the SNS environment, and thus the effective $\nu_e C$ event rate per year is expected to be about 900 events. From the above considerations it is quite obvious that the size of the fiducial volume of the homogeneous detector is an essential factor in obtaining reasonable event rates. Therefore, we shall continue to investigate other, less intrusive PMTs as an alternative to the proposed Hamamatsu R5912 phototubes, as well as other compact photodetection devices.

Our cost estimate for the homogeneous detector is approximately M$1.44, as follows: $1,300 per channel (PMT + QT electronics) = M$0.78 and M$0.25 for the tank, DAQ, and laser calibration systems, for a total of M$1.03. Assuming a 40% contingency, this yields our total estimated cost of M$1.44.

Appendix-V

Segmented detector

Detector Description

The geometry and principle of operation of the segmented detector are similar to those of the Soudan-II proton decay experiment. The detector is composed of passive absorber assembled from thin wall tubes, each containing a straw tube gaseous detector as the sensitive medium. The signal would be read out from both ends of each individual tube from the central resistive wire. Such a detector configuration provides flexibility to use the same sensitive part with various absorber materials, and therefore use the same detector with different targets. As a result, neutrino interactions with different nuclei can be studied without construction of a completely new detector every time. A transverse cut of the one of the possible detector schemes is shown on Figure 1.

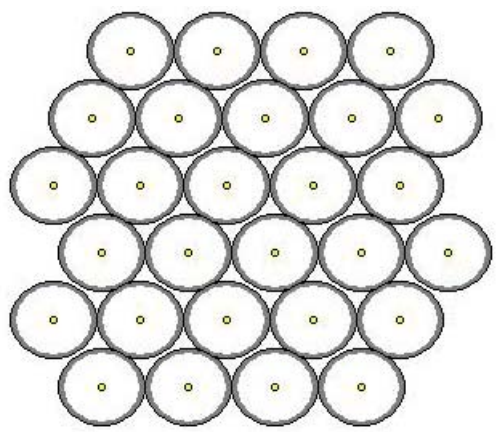

Figure 1. Schematic cross cut view of the proposed segmented detector. Dark color is the absorber/target pipes. Straw tubes are inserted. Only the central readout wire for the straw detectors is shown.

The particle energy in such a detector is reconstructed by measurement of the range of the particle track or by the total number of fired cells. Directional information can be extracted from the reconstruction of the three dimensional information, X and Y coordinates from straw tube position and Z coordinate by comparing amplitude of the signal from two opposite ends of the same straw tube.

Detectors with straw tubes as the sensitive elements have a number of advantages compared, for example, to those with higher density sensitive elements such as scintillator rods. In general, straw tubes are less expensive, and do not require a complex light-readout system. In addition, the lower mass of the sensitive part of the detector

relative to the absorber (target) mass eliminates the necessity to subtract interactions in the detector active medium. The energy range of electrons from neutrino nucleus interactions at the SNS is a few tens of MeV. Those energy electrons can be treated as minimum ionization particles with a low probability of energy loss via bremsstrahlung. As a result, energy measurement by the track range could be as good as by total energy deposition.

The design of such a detector needs to be a reasonable compromise between cost and performance. The thinner the tube walls, the longer the track length and less energy loss in the passive absorber. This results in better energy and angular resolution. On the other hand, thinner tube walls give the detector less average density and drive up the size and the number of channels. We obtained an initial optimization of the detector using a GEANT Monte Carlo code. For the detector optimized to measure neutrino-iron cross sections as a reference point we can use as absorber iron pipes with 15 mm outer diameter and 13.5 mm inner. Straw tubes can be made of carbon coated Kapton as the inner layer with a laminate Kapton and Aluminum foil as outer layer. Total wall thickness is 0.1 mm and the outer diameter is 13 mm.

To estimate the necessary size of such a detector using for example an iron absorber we assume that the ν-Fe cross section is $2.6 \cdot 10^{-40}$ cm^{-2}. At 20 meters from the SNS target for a 1 MW, 1 GeV SNS proton beam, the neutrino flux is 10^7 neutrinos cm^2 sec^{-1}. For a desired event rate of 10 neutrino interactions per day and 40% event reconstruction efficiency it is necessary to have a total mass of iron targets in the detector of 10 tons. To achieve this mass required a total fiducial size of the detector of $(2\ m)^3$. With a minimum size if the dead volume at the edges of detector is 10 cm, we need the total detector dimensions of $(2.2\ m)^3$. To instrument such a detector we need ~21 thousand, 2.2 meters long straw tubes. The absorber will consist of 21 thousand, 2.2 meters long iron pipes. Some future optimization in reduction in the number of read out channels is possible if the overall geometry of the detector is changed from cubical to rectangular. This can be done after the exact geometry of the detector footprint inside the neutrino bunker is available. In general such a detector design is quite flexible to configuration changes and has the possibility to fit on almost any footprint.

Monte Carlo Simulations

During the Monte Carlo study of the segmented detector we compared two types of active elements for the detector, scintillation rods, and gaseous drift tubes. The results of the simulation, for 30-MeV electrons for both gas tubes and scintillation rods, are shown in Figure 2. For this simulation, an ideal light readout (no photo-electron statistical fluctuations) was assumed.

For the scintillator as an active medium the electron energy resolution by measurement of the total energy deposition in the scintillator is 21.4%; the energy resolution measured by track range is 23.4% as shown on the upper two graphs on Figure 2. For a realistic detector, energy resolution reconstructed by energy deposition will be significantly worse because of the unavoidable contribution from the photoelectron statistical fluctuations in the light collection system.

On the lower part of the figure, the simulation of the detector with gas tubes is shown. The average number of fired cells is slightly less and resolution is slightly worse for straw tube detectors compared with scintillator, because of the lower efficiency for low-energy photons, which are converted and absorbed mostly in the material of absorber.

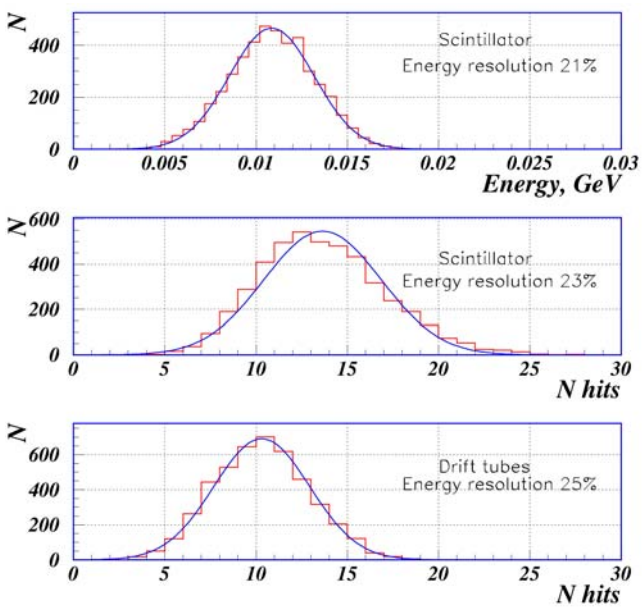

Figure 2. Detector energy resolution shown, for scintillator and gas drift tube as sensitive volumes. Energy is reconstructed by measurement of total energy deposition in scintillator (upper figure), by the number of fired cells for scintillator (middle figure), and by number of the fired gas drift tubes (lower figure). The electron energy is 30 MeV. For the upper figure an ideal light readout (no photo-electron statistical fluctuations) was assumed.

For electrons with energy below 50 MeV the probability to start an electromagnetic shower is negligible. As a result, measurement of the energy using the number of fired cells has excellent linearity as can be seen in Figure 3.

Figure 4 shows results of simulations of energy and angular resolution for various energy of electrons for two sets of absorbers. One set with diameter 20 mm and 1 mm thick walls and a second with diameter 10 mm and 0.5 mm walls. The average density of the detector is the same for both sets, so it does not change the overall detector size. As one can conclude the detector with 10mm absorber has no advantage for the angular resolution and slightly better energy resolution then the detector with 20 mm absorber. Larger

absorber tube diameter and wall thickness significantly reduces the number of read-out channels and overall detector cost. Future simulations and R&D will let us optimize cost/performance ratio.

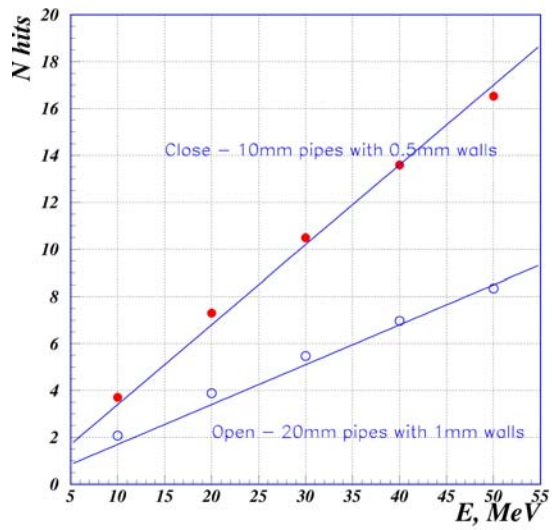

Figure 3. Dependence of the electron energy relative to the number of hits for the segmented detector with a gas as active media. Simulation results for two different absorber thicknesses are shown. The detector has good linearity because electrons in this range of energies behave as minimum ionizing particles.

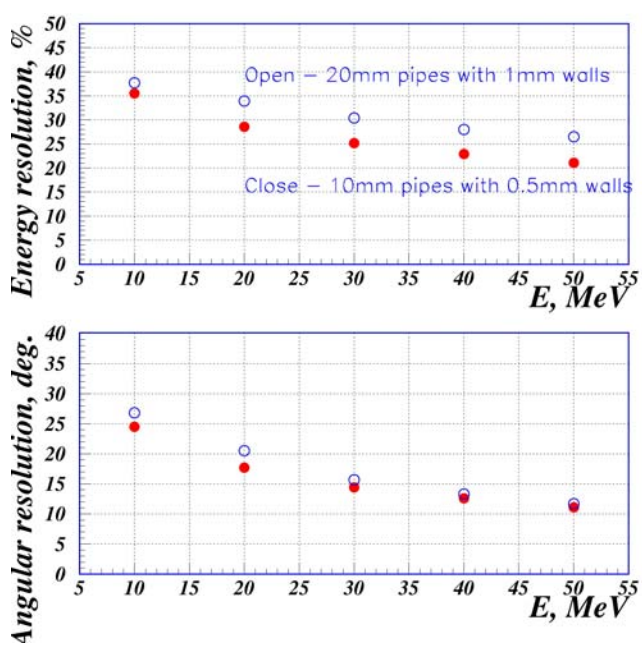

Figure 4. Energy and angular resolution for the segmented straw tube detector for two different absorber tube thickness and diameters.

The major source of beam-correlated background for neutrino interactions at stoped pion facilities is interactions of high-energy neutrons produced in the SNS target and penetrating inside the detector bunker. Their interaction might knock out a proton which could imitate the track of an electron. However, recoil protons always have a kinetic energy below the maximum energy that the neutron can have at the SNS, or below 1 GeV. For this energy range, protons are not in the minimum ionization region and to produce the same number of hits as an electron, the proton mast have a much higher energy as seen in Figure 5.

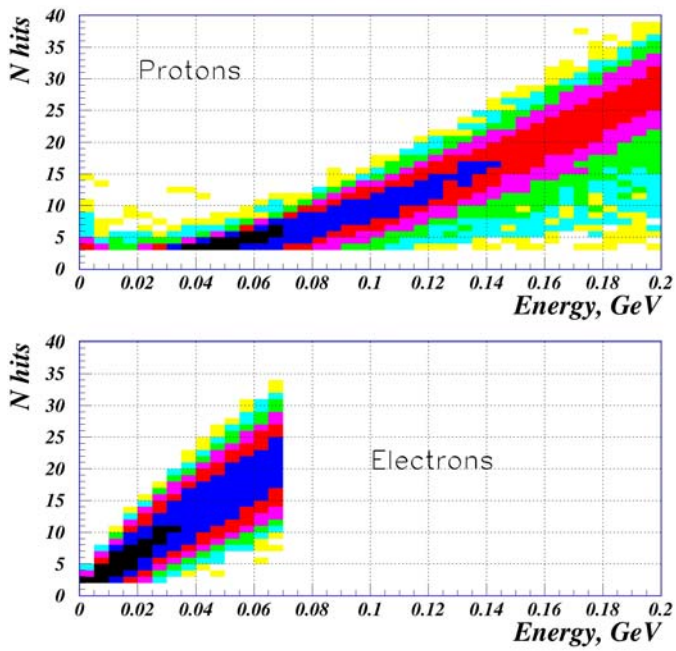

Figure 5. Average number of hits for electrons and protons of various energies. Absorber - 10mm diameter 0.5 mm walls. Detector – gas straw tubes. To produce the same number of hits protons must have much large kinetic energy then electrons.

For example, a 140-MeV proton produces the same number of hits as a 35-MeV electron. Because the majority of the neutrons at the SNS has a relatively low energy, corresponding recoil protons have low energy as well. Cut off in the hit numbers in detector efficiently eliminates this source of background. In addition, it is possible to separate electrons from protons with the same number of hits by the shape of the track. The proton tracks are more linear, and the electron tracks are irregular in shape because of the emission of photons and their conversions. In Figure 6, examples of the event topology, for 40-MeV electrons and 125-MeV protons are shown. By the introduction of the "track linearity parameter," which is the “goodness” of how well one can fit the track

with a straight line, one can separate electrons from protons even if they produce the same numbers of hits. This feature is shown on Figure 7, and Figure 8.

A significant extra rejection factor will be obtained from an amplitude analysis of the signals. More sophisticated algorithms developed after addition simulations and R&D will improve the background rejection even further.

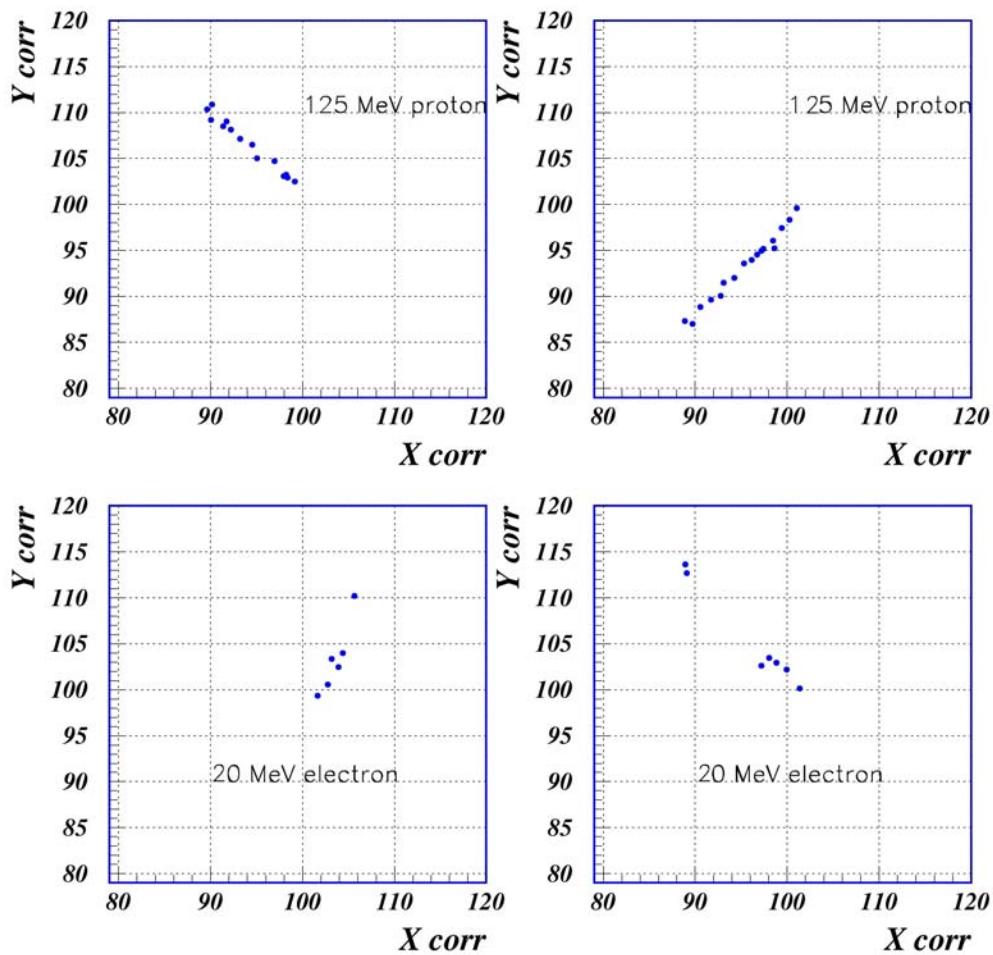

Figure 6. Examples of the simulated hits topology for the 20 MeV electrons and 125 MeV protons. Coordinate units are straw tube number. Proton track are more linear and more dense than electrons.

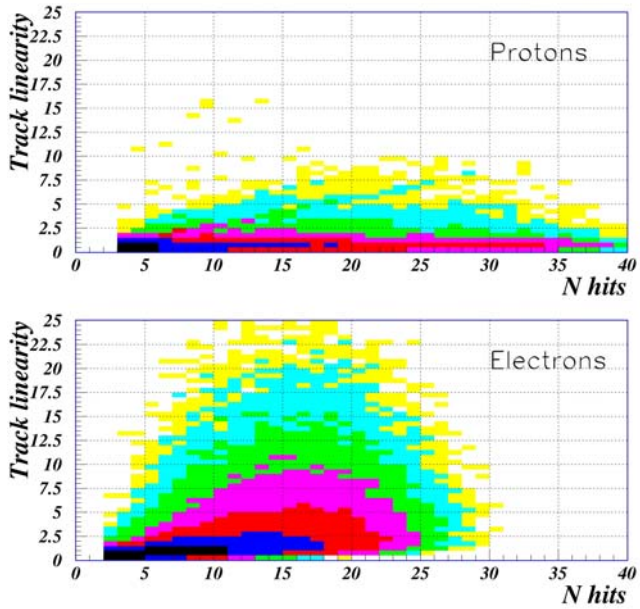

Figure 7. Track linearity, goodness of the liner fit, for 40 MeV electron and 125 MeV protons. Average value of the track linearity parameter for protons is significantly lower than for electrons.

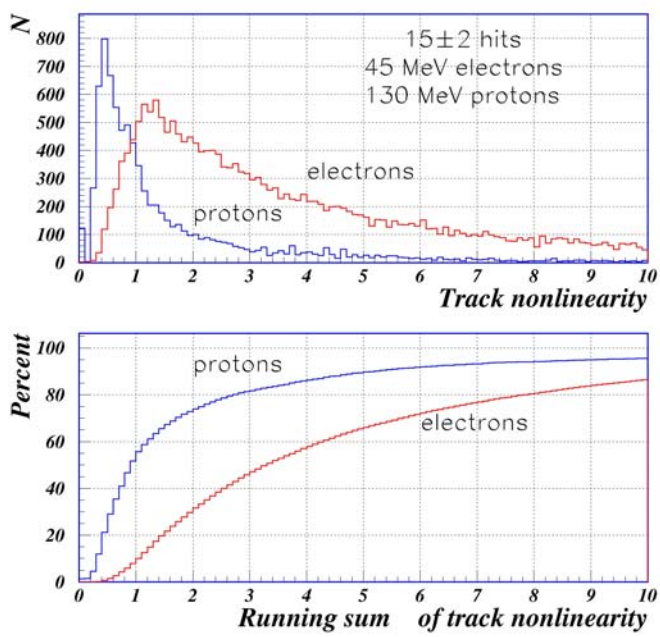

Figure 8. Separation of the protons from the electrons using only the track linearity parameter. A cut of "1" in non linearity, eliminates 60% of protons but keeps electron efficiency better then 90%

Conclusion:

A segmented detector based on gaseous straw tube sensitive elements has excellent performance for identifying neutrino interaction events. The flexible geometry for this type of detector allows its dimensions to be optimized for the final ν-SNS bunker size. The reusable nature of the sensitive elements allows the measurement of different targets with the same detector, reducing systematic errors and costs. Construction of such a detector will let to start a program of study of neutrino interactions with various targets.

The detector has very good linearity, energy and angular resolution, and low mass of the sensitive part.

Preliminary top-level cost estimations:

Straw tubes	$20 tube –	$400K
Electronics	$50 tube -	$1000K
Design and Mechanical Support -		$200K
Assembly	$10 tube	$200K
Gas system		$100K
Initial set if iron targets		$400K
Total:		$2400K

Appendix-VI.

Cosmic Veto system

For the neutrino detector and shielding enclosure a space of ~ 4.5m · 4.5m with a clear height of 6.5m would be available in the SNS target hall. The cosmic ray muon flux through this volume is estimated to be ~ $2.5 \cdot 10^8$ events per day. Such cosmic ray events must be suppressed through a combination of the SNS time structure, an active veto counter, shielding and detector signature.

The SNS time structure (~700 ns proton pulses at 60 Hz) reduces the effective cosmic ray muon flux through this volume to $1 \cdot 10^5$ events per day. The passive shielding will have to take care of the neutral components of the background as an active veto system only can provide rejection for the charged component of the cosmic background. Additional rejection can be expected from the signatures of the muons in the inner detector.

We are aiming at a design of a cosmic veto system with an efficiency of better then 99%. Contributing to this efficiency is predominantly area coverage and detection efficiency of the energy deposited in the choice of detector.

The experiences with the cosmic veto detector of the KARMEN experiment as described in [1] give us a starting point for our design. KARMEN achieved initially an area coverage of about 99%, but experienced additional leakage through the need to set a lower energy limit on the muon peak to avoid the overlap with the gamma peak from natural background radiation.

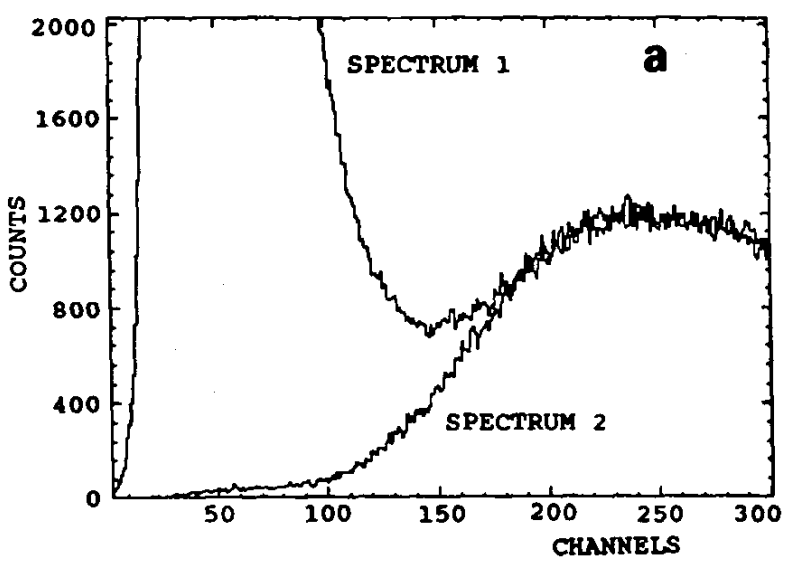

Fig. 1: Energy spectrum of the muon veto counter of the KARMEN experiment.

In Fig. 1, spectrum 1 shows both the strong low energy gamma background and the muon peak, while spectrum 2 contains only the simulated muon contribution. As a too low

threshold in the energy spectrum would lead to too high a dead time for the detector it has to be determined what the effect of the threshold is on the efficiency of the veto. Based on the simulation the KARMEN group calculated the total leakage as a function of the threshold as shown in Fig. 2.

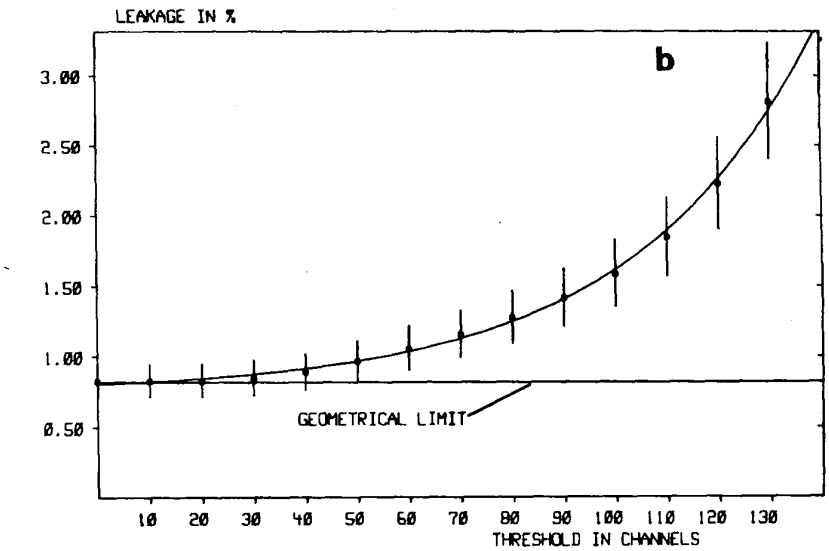

Fig. 2: Dependence of detection leakage on lower threshold as set in Fig. 1.

The graph shows that for the type (NE-110) and thickness (3 cm) of plastic scintillator used the gamma/muon separation is barely sufficient. Allowing a total of 1.5% leakage the KARMEN experiment had to experience about 10% false vetoes from the gamma background. This number would rise dramatically if the threshold would be lowered further. As a positive result from the type of scintillator used, the group reported further that the energy resolution of the muon signal remained nearly constant over the length (distance to the photomultiplier) of the scintillator sheet (300 cm). In a later stage the KARMEN experiment added an additional scintillator veto within their shielding consisting of 5 cm thick plastic material to further improve on their cosmic veto. Overall they achieved a cosmic muon rejection of 99.6%.

Based on the KARMEN results we are planning to use a similar scintillation material (EJ-200, EJ-208 or BC-408, BC-412) with a thickness of 1.5” (3.81 cm) in order to improve on the gamma/muon separation compared to the results in Fig. 2 of the initial KARMEN setup. We should also be able to improve on the geometrical coverage by using a second layer of detectors to cover edges and gaps between sheets and easily reach the aim of better than 99% efficiency for the cosmic muon veto.

A further decision to be made is the layering of the active veto in relation to the passive shielding. If the active veto could be mounted on the inside of the massive iron shielding, the necessary amount of scintillation material could be reduced. In order to investigate this point we conducted Monte Carlo simulations using the GEANT-4 code (see e.g. Fig. 3). Muons (with energies ranging up to 1000 GeV) were simulated incident

on a simplified version of our planned setup which consisted of 1 m iron sheet on top and 0.5 m iron walls, an inner veto detector and a central detector filled with liquid scintillator. We required a minimum energy deposit of 1 MeV in the veto and a 2 MeV deposit in the central detector, thus counting an event as a failure when a larger than 2 MeV deposit showed up in the central detector without an accompanying veto.

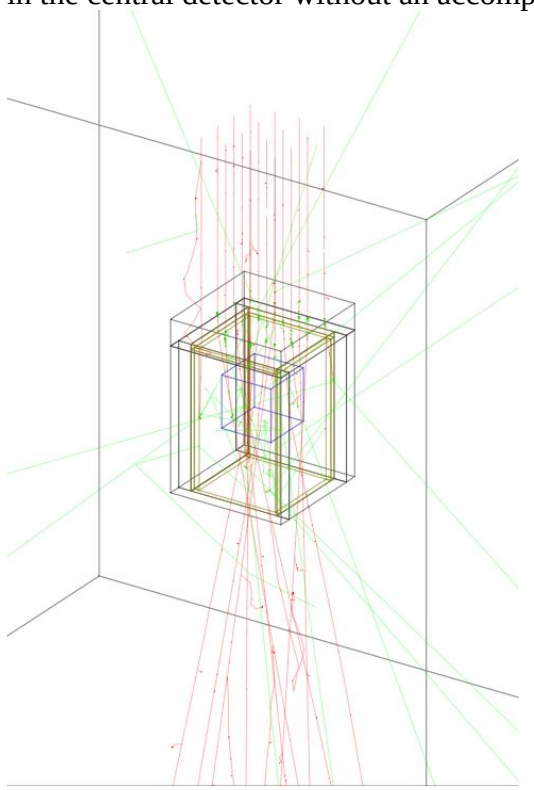

Fig. 3: GEANT-4 layout of simplified setup for simulation of veto leakages.

Our simulations showed that the arrangement with the veto scintillator on the inner side of the shielding leads to failures to detect the muon when the muon itself does not pass the scintillator but produces neutrals in the iron shielding that reach the central detector. This effect was also observed by the KARMEN experiment and led to the installation of the additional veto counter inside the shielding. In order to avoid this leakage we are now planning to place the cosmic muon veto on the outside of our massive iron shielding. Secondary neutral particles can still be produced in the surrounding material, but after passing the veto undetected they still have to traverse the iron shielding to reach the central detector. Monte Carlo simulations with this modified setup (Fig. 4), now also including a concrete floor and concrete shielding of the SNS primary beam line are ongoing. We will incorporate more experimental details of the setup and the SNS environment once they become available to us as well as run other components of cosmic radiation through our simulation.

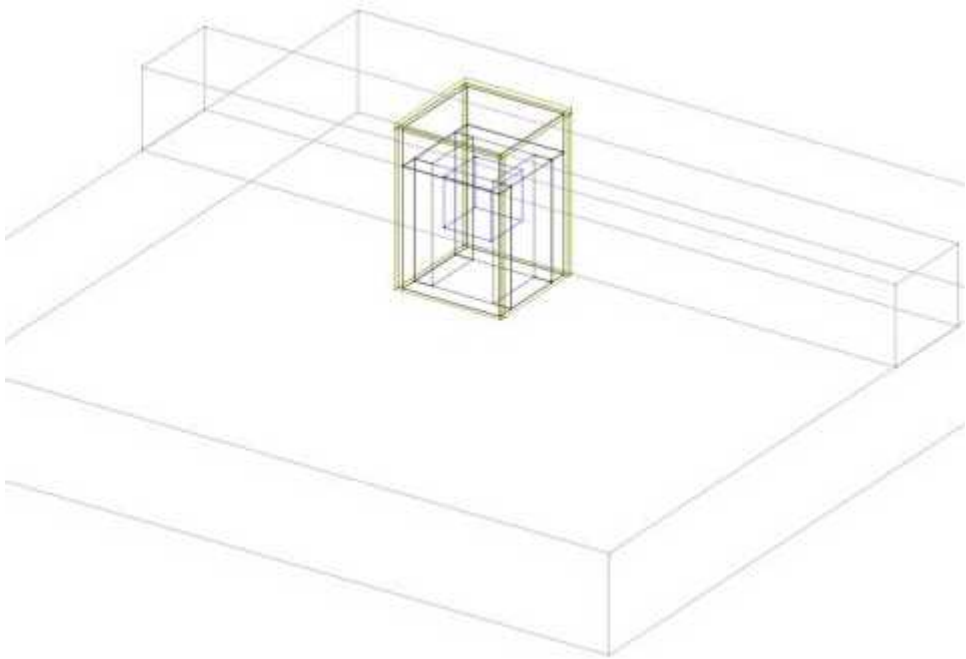

Fig. 4: Modified setup for GEANT-4 simulations of the veto leakage

For the actual layout of the individual plastic scintillation "paddle" we want to follow a design used by the Pion Beta collaboration at the Paul Scherrer Institute in their cosmic veto counter [2].

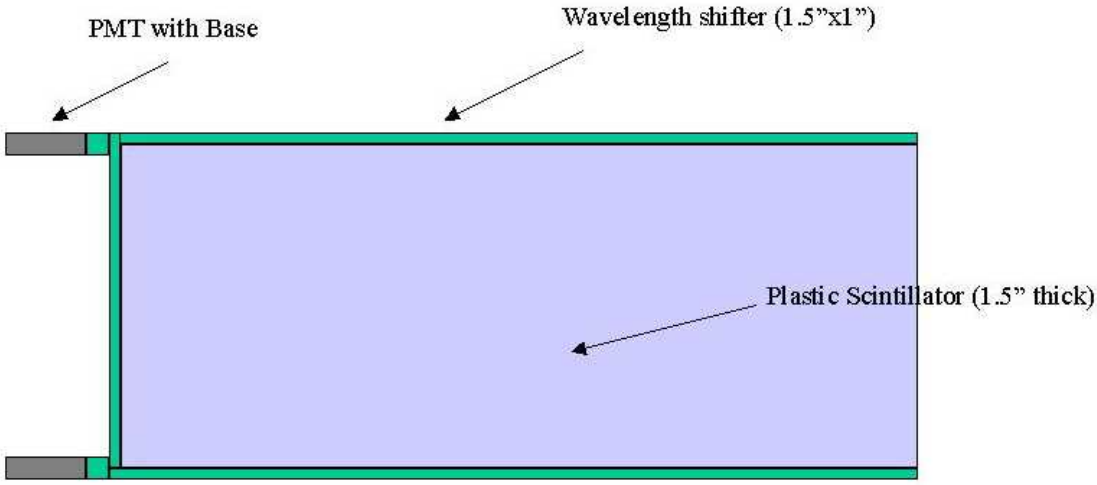

Fig. 5: Schematic drawing of the makeup of one scintillator "paddle" which is supposed to cover an area of app. 0.75 m x 2.25 m.

In their design they use relatively large area plastic sheets that are read out through wavelength shifting scintillator strips along the sides (schematic representation in Fig. 5). The use of relatively large sheets should enable us to limit the area of gaps that will need to be covered by a second layer of smaller (narrower) sheets. We limit the size of one "paddle" to app. 0.77 m x

2.25 m as it will be with a weight of roughly 90 kg still reasonably easy to handle in the mounting process. For the first layer of sheets we need 76 “paddles” with a total weight of nearly 6.8 tons and 152 electronic channels for the readout. For the second layer detectors we anticipate the use of narrower sheets but a similar number of electronic channels (98). Total weight of the detector will be thus nearly 9 tons employing 250 electronic channels.

The limited space at the SNS location and the need for a second layer of scintillator sheets to cover gaps will require use of a deflected readout from the wavelength shifter strips into the photo multiplier tubes (PMT’s). A possible schematic layout is shown in Fig. 6.

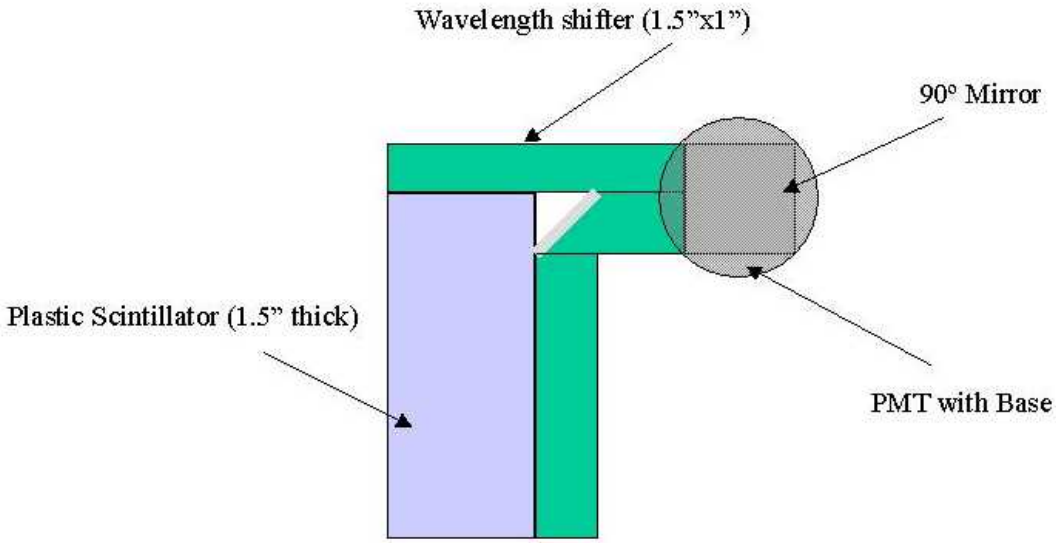

Fig. 6: Schematic layout of a mirror solution for the angled readout of the “paddles”.

A layout of this type was also used for the Pion Beta experiment at PSI and the efficiency of the deflected readout was compared with a straight readout (Fig. 7). Although some losses are incurred the muon signal still remained strong and nearly no loss in resolution was incurred. This part of the light readout will have to be developed at the Colorado School of Mines (CSM) as it is not commercially available yet. The detector “paddles” will be of different height to allow staggering of the PMT readout in places where they would otherwise overlap. It is planned to have the detector paddles built completely by a suitable vendor after the testing and development of prototypes at the Colorado School of Mines has been completed. Delivery of the final detectors should be directly to ORNL where our team will provide quality control before the installation. The electronics setup will be developed and tested at CSM.

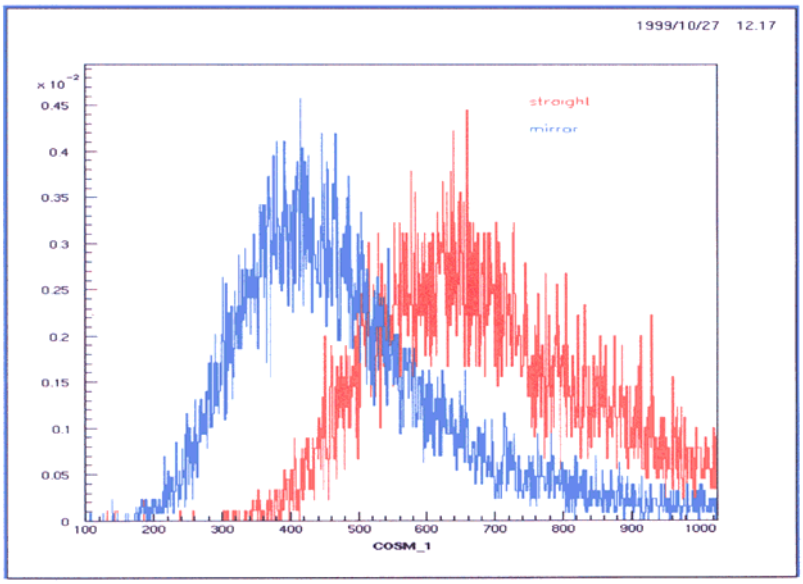

Fig. 7: Comparison of the muon energy spectrum of a plastic scintillator "paddle". In red the straight readout, while the 90° deflected spectrum is shown in blue.

Budget:

The budget is based on first inquiries with selected vendors. Alternatives will be investigated and will hopefully reduce the cost estimates.

Scintillation detectors (including PMT's and bases): $ 700k
Mounting Materials (estimated at 10% of detector cost): $ 70k
Electronics (250 channels , includes cables): $ 200k
Necessary R&D for detector angle readout, prototype testing, construction design, quality control and mounting: $ 230k
Total cost for the veto project (without contingency): **$ 1,200,000**

References:

1. B. Bodemann et al., Nucl. Instrum. Meth. A 286 (1990) 214
2. http://pibeta.web.psi.ch/subprojects/cosmic_veto/cosmic_veto.html

Appendix-VII

Neutrino Bunker and Floor Loading

At full power (1.0 MW) the SNS will bombard a mercury target with a 1.0 mA, 1.0 GeV proton beam, producing ~0.1 neutrinos per proton in short bursts. The resulting neutrino flux at the detector location will be ~$1.0 \cdot 10^7$ ν/s/cm^2 of each flavor, providing several tens of neutrino interactions per day for a ten ton detector. This must be compared with the cosmic ray muon [neutron] flux through this volume of ~$2.5 \cdot 10^8$ [$1.4 \cdot 10^6$] events per day; and machine-related backgrounds - primarily neutrons with an energy spectrum shown in figure 1 – which contribute an additional ~10^{10} events per day. These background sources must be suppressed through a combination of the SNS time structure, particle identification (discussed in Appendices IV and V), an active veto system (discussed in Appendix VI), and shielding.

The backgrounds of most concern are those which can lead to a high-energy neutron inside the detector volume, which can in turn leave a signature indistinguishable from a neutrino-nucleus interaction. These types of events will arise from three primary sources:

Cosmic Ray Muons

The flux of cosmic ray muons through the detector volume is roughly $2.5 \cdot 10^8$/day. The SNS time structure (~700 ns proton pulses at 60 Hz) allows us to eliminate a large amount of this type of background by turning off the detector except for the small fraction of time during which neutrinos can come from the target. Target neutrinos, which result from the $\pi \rightarrow \mu \rightarrow \nu$ decay chain, will all arrive within several muon decay lifetimes (τ_μ = 2.2 μs). This results in an active time of only $4 \cdot 10^{-4}$ seconds for every second of machine operation, thus reducing the effective cosmic ray muon flux through the detector volume to $1 \cdot 10^5$/day. Two more orders of magnitude reduction are provided by the active veto, leaving 1000/day untagged cosmic ray muon events. To a good approximation, we are only concerned with those muons that produce a neutron in the last interaction length of shielding. The observed $\mu \rightarrow n + X$ yield is $4 \cdot 10^{-5}$ n/μ/(g/cm^2), giving ~5.2/day neutrons generated in the shielding enclosure by cosmic ray muons which failed to fire the active veto system. Finally, these events are further suppressed by particle identification measures in the detectors themselves (Cherenkov light in the homogeneous detector; track linearity and density of energy deposition in the segmented detector).

Cosmic Ray Neutrons

Cosmic ray neutrons, with an incoming flux of $1.4 \cdot 10^6$ /day, are similarly reduced by the SNS time structure to ~560/day. The active veto does not help with this background source, but shielding does. In order to reduce this source by ~ two orders of magnitude (making it approximately equal to the irreducible neutron background from untagged cosmic-ray muons) a meter of steel shielding is required for the enclosure roof.

The cosmic ray flux is lower through the enclosure sides, and only ~ half-meter walls are required. As with the previous background source, this one is further reduced by applying particle identification techniques.

Machine-related Backgrounds

Machine-related background is primarily in the form of neutrons, whose energy spectrum is shown in figure 1. There are large uncertainties in this background because shielding of nearby neutron-scattering instruments is not finalized yet. However, we believe the fluxes shown in figure 1 correspond to worst-case scenarios, both for scattering off nearby instruments and for proton beam losses.

Once again the SNS time structure is important for reducing backgrounds. The slowest neutrons (E_K < 0.038 MeV) arrive after the neutrino pulse. The fastest neutrons (E_K > 3.4 MeV with a τ < 0.7 μsec) arrive earlier than most electron neutrinos, which are delayed by the characteristic muon lifetime (2.2 μsec). Those neutrons can be eliminated by applying 0.7 μsec time cut. Remaining neutrons have such low energy that they are eliminated by the detector response. Note however: for neutral current measurements it would be advantageous to be able to run without this τ_{min} cut because during the initial 0.7 μsec the neutrino flux is dominated by muon neutrinos resulting from pion decay so that the neutral current events do not need to be separated from a charged current background. Our ability to handle the facility backgrounds without this time cut will require additional studies and shielding optimization which can be made when shielding details of surrounding neutron scattering instruments are finalized.

Bunker Volume/Weight and SNS Floor Loading Capacity

The detector volume identified on the SNS target building floor is ~4.5m · 4.5m · 6.5m. The required shielding leaves a facility volume of 3.5m · 3.5m · 5.5m which can be instrumented. This is sufficient to house the active veto system and two neutrino target/detector systems. The weight of the shielding is ~350 tons. Together with the weight of the detectors and the veto system (< 40 tons) this is within the minimum floor capacity as determined by the engineering firm m+w zander (SNS Target Building designers) as documented in the attached report. Additionally, this report shows that with administrative controls preventing loads in the aisleway between **ν-SNS** and flight-path 18, an additional 150 tons of shielding could be safely accommodated.

Cost Estimate

We estimate the total cost of the bunker to be $500,000 primarily machining and installation of steel volumes.

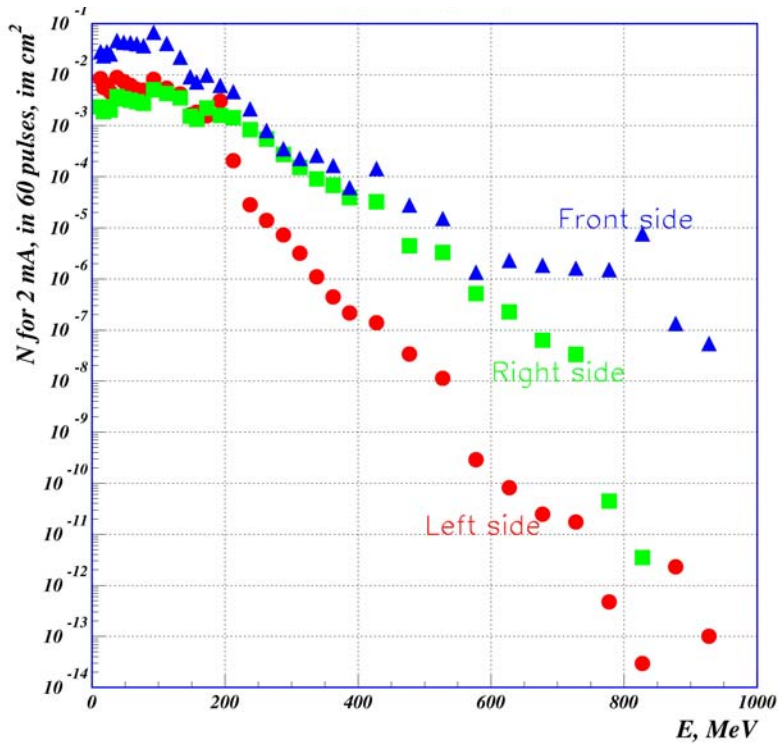

Figure 1. Machine-related neutron spectra entering neutrino enclosure from the front (facing Spallation target), the right side (adjacent to the proton beamline), and the right side. Fluxes (in neutrons/cm^2/sec) scale linearly with SNS beam power (assumed here to be 2 MW). For these calculations we assumed worst-case scenarios for the neighboring flight-path shielding configuration and the maximum allowed beam losses in the high-energy proton tunnel. No time cut on the neutron appearance has been applied.

m+w zander

total facility solutions

DEPARTMENT OF ENERGY

NEUTRINOS AT THE SPALLATION NEUTRON SOURCE (ν-SNS)
OAK RIDGE NATIONAL LABORATORY

OAK RIDGE, TENNESSEE

FLOOR LOADING REPORT

Subcontract Number: 4000029836
Project Number: 10241

FEBRUARY 25, 2004

JENOPTIK Group.

m+w zander
total facility solutions

M+W Zander U.S. Operations, Inc.
549 West Randolph Street
Chicago, Illinois 60661
USA
Phone +312-577-3200
Fax +312-577-3525

February 25, 2004

Vince Cianciolo
MS 6356
Oak Ridge National Laboratory
Oak Ridge, TN 37831-6356

Dear Vince:

M+W Zander has completed the floor loading review for the proposed Neutrino enclosure to be located in the SNS Target Building. This study has been undertaken due to the desire to place a Neutrino Detector and Shielding in an area of the Target Building that has an allowable load criteria of 1500 psf. Calculations have been prepared to review the floor and foundation load capacities and to determine the feasibility of increasing the allowable loads. The allowable load for the Neutrino Detector and Shielding and a description of the load assumptions is given below. The calculations are on the following pages.

Case 1 – 395 Tons
Load is assumed to be applied to the footprint of the enclosure. There is no reduction in the live load of 1,500 psf outside the enclosure.

Case 2 – 470 Tons
Half of the 5' width surrounding the enclosure is maintained as a "keep clear" area. Load capacity is reduced in that width to 100 psf with the remaining load capacity assigned to the Neutrino Detector. The area beyond 2.5 feet has a floor load of 1,500 psf.

Case 3 – 545 Tons
The entire 5' width surrounding the enclosure is maintained as a "keep clear" area, load capacity is reduced in that width to 100 psf and all of the remaining load capacity is assigned to the Neutrino Detector. The area beyond 5 feet has a floor load of 1,500 psf.

If either Case 2 or Case 3 is used for designing the Neutrino Detector, we recommend that the "keep clear" area be striped and marked. If Case 3 is used, the Beamline 18 group should be informed that the Neutrino Detector has claimed all of the load for the "keep clear" area.

If you have questions, please do not hesitate to contact us.

Very truly yours,

M+W ZANDER U.S. OPERATIONS, INC.

John J. Busch, SE, PE
Senior Project Manager

G. P. Reddy, SE
Structural Project Engineer

1. Introduction

The proposed location of the Neutrino enclosure is on the pit floor of Instrument No. 18, along column line G between column lines 1 and 2.5. This area is adjacent to the RTBT enclosure. See attached sketch SK-1 for layout. Location and size of the enclosure has been provided by Vince Cianciolo of ORNL. The proposed enclosure is constructed of solid steel plates and for purposes of analysis, 355 tons is used for the weight of the enclosure. Inside the enclosure are two neutrino detectors, each weighing 20 tons.

The equivalent uniform floor load is calculated as follows:

Weight of steel plate enclosure: 355 tons = ... 710,000. lbs
Weight of two neutrino detectors: 2 x 20 tons = 40 tons = ... 80,000. lbs.
Total weight of Neutrino enclosure =..... 790,000. lbs. = 395 tons
Floor area of enclosure is 219 sq. ft.
Equivalent uniform floor load equals = 790,000 / 219 = 3,607 psf
USE 3,600 psf

2. Pile Capacities

The existing pit floor consists of an 18 inch thick reinforced concrete slab, supported on a compacted layer of stone, 12.5 feet thick, which is supported on a 5 ft thick reinforced concrete mat. The mat is supported on grouted steel pipe piles, which bear on bedrock. The design pile load capacity is 200 tons with a factor of safety of 2. See sketch SK-2 for layout of piles.

The piles under the Target Building are designed for vertical gravity dead and live loads as well as seismic vertical and lateral loads. The design live load for this area is 1,500 psf. The Neutrino load of 790,000 lbs. is distributed at a 2 vertical to 1 horizontal slope to the foundation piles. Two load cases are considered to determine the vertical pile loads: 1.) Total Static Load = Dead Load + Live Load + Neutrino Load and 2.) Total Dynamic Load = Dead Load + Seismic Live Load + Neutrino Load + Earthquake. The attached spreadsheet shows the existing pile loads and the additional loads from the Neutrino detector enclosure.

The maximum vertical pile load for the two load cases are as follows:

Total Static Load = 421 kips > 400 kips with factor of safety of 2.0
= 421 kips with factor of safety of 1.9 – Okay.
Total Dynamic Load = 502 kips < 400 x 1.33 = 532 kips – Okay. 1.33 is allowable load increase for seismic.

3. "Keep Clear" Area

The "keep clear" area is designated as an open area, 5 feet wide, in which the floor live load is 100 psf. See sketch SK-1. The reduction of live load of 1,400 psf (1,500 – 100) multiplied by the "keep clear" area (216 sq. ft.) is 300,000 lbs or 150 tons. This portion of the live load can be added to the weight of the Neutrino enclosure. Case 1 - No "keep clear" area. The total weight of the Neutrino enclosure is 395 tons. Case 2 - One half "keep clear" area. The total weight of the Neutrino enclosure is 470 tons. Case 3 - Entire "keep clear" area: The total weight of the Neutrino enclosure is 545 tons. In our opinion, the pile load from Cases 2 and 3 are within the allowable factor of safety and further analysis is not needed.

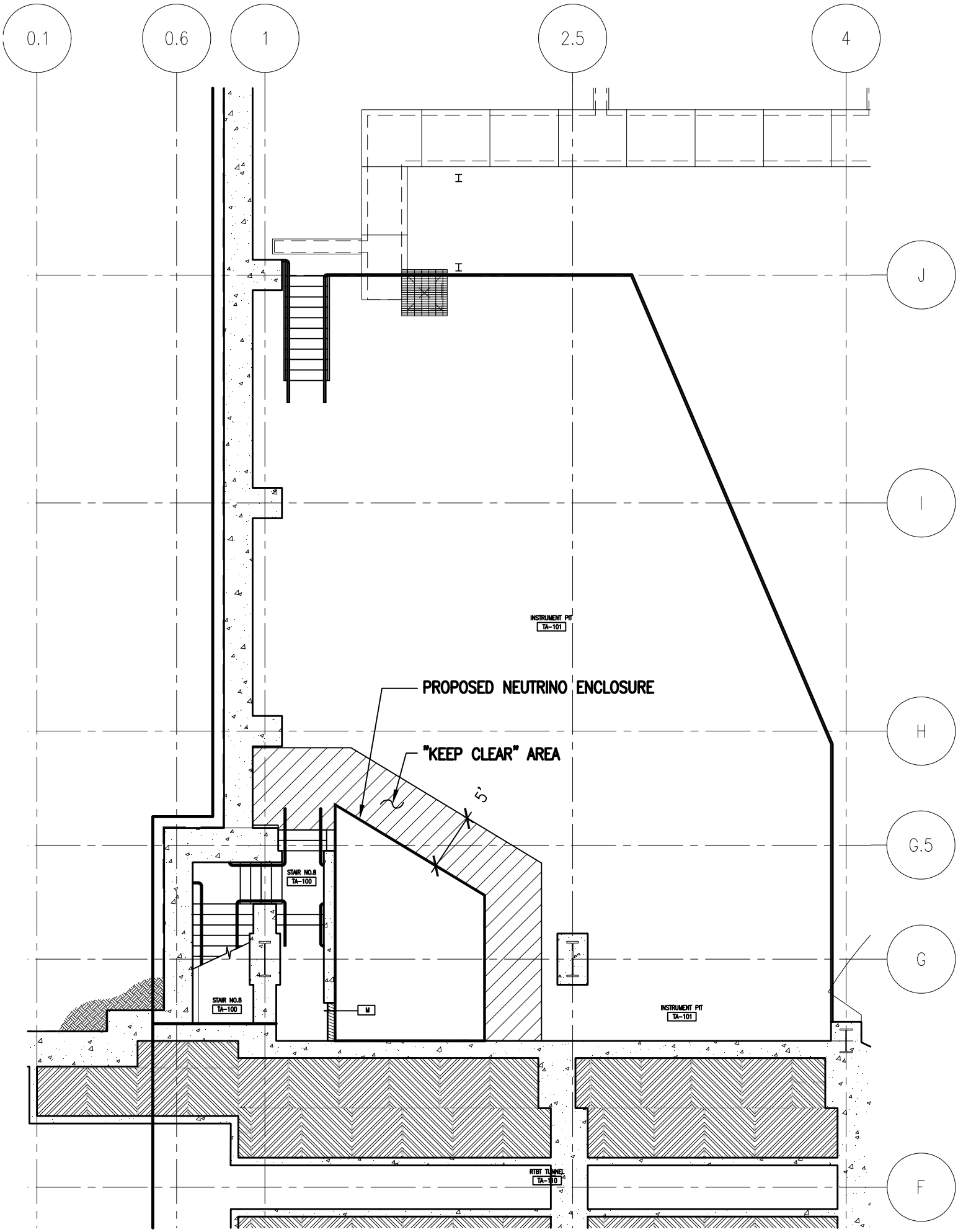

INSTRUMENT LEVEL SECTOR 41

EXTRACTED FROM A2.01.41 R.3

SK-1

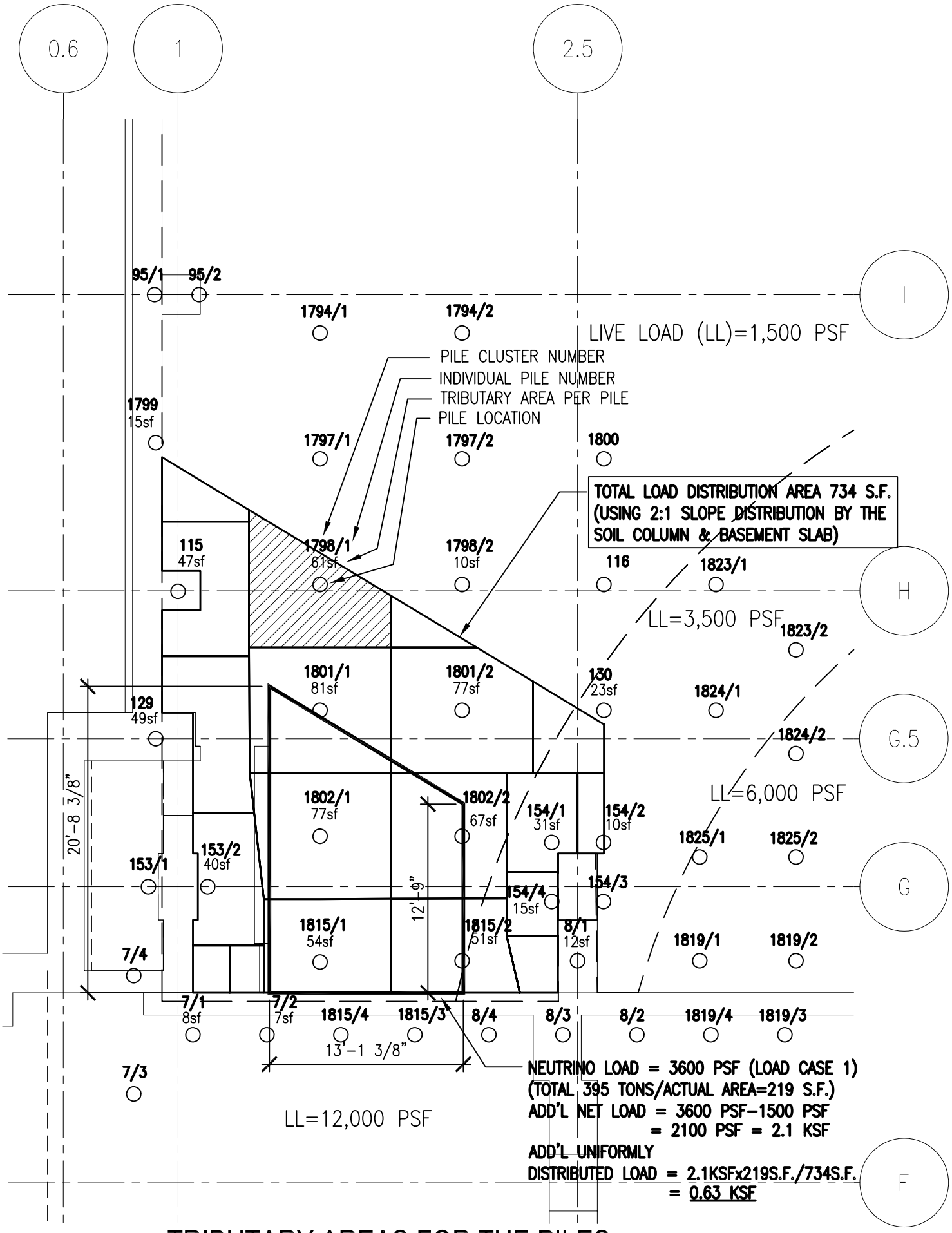

TRIBUTARY AREAS FOR THE PILES

BASED ON KNIGHT DWG. NO. S1.FP.30 R.4C

SK-2

SNS NEUTRINO PILE LOAD TABLE (See Next Page for Notes)

Cluster Node a	No. of Piles b	Individual Piles c	Loads per SDE-00-09-28-C-007(App.F&G) DL + LL Total Vertical Load (k) d	DL + LL Vertical Load per Pile (k) e=d/b	DL + SLL + EQ Vertical Load per Pile (k) f	Additional Loads from "Neutrino" Uniform DL + LL Load (ksf) g	Area per Pile (sf) h	Add'l Load DL + LL per Pile (k) i=gh	Total Static DL + LL + Neutrino per Pile (k) j=e+i	Add'l Load From Vertical Seismic .24xNeutrino per Pile (k) k=0.24i	Total Seismic DL + SLL + EQ + Neutrino per Pile (k) l=f+l+k
7	4		1502								
		7/1		375	447	0.63	8	**5**	**380**	**1**	**453**
		7/2		375	447	0.63	7	**4**	**380**	**1**	**452**
8	4		1587								
		8/1		397	460	0.63	12	**8**	**404**	**2**	**469**
		8/2		397	460	0.63	0	**0**	**397**	**0**	**460**
		8/3		397	460	0.63	0	**0**	**397**	**0**	**460**
		8/4		397	460	0.63	0	**0**	**397**	**0**	**460**
115	1		377	377	458	0.63	47	**30**	**406**	**7**	**495**
116	1		391	391	452	0.63	0	**0**	**391**	**0**	**452**
129	1		376	376	453	0.63	49	**31**	**407**	**7**	**491**
130	1		386	386	449	0.63	23	**14**	**401**	**3**	**467**
153	2		749								
		153/1		374	448	0.63	0	**0**	**374**	**0**	**448**
		153/2		374	448	0.63	40	**25**	**400**	**6**	**479**
154	4		1555								
		154/1		389	453	0.63	31	**20**	**408**	**5**	**477**
		154/2		389	453	0.63	10	**6**	**395**	**2**	**461**
		154/3		389	453	0.63	0	**0**	**389**	**0**	**453**
		154/4		389	453	0.63	15	**9**	**398**	**2**	**465**
1798	2		736								
		1798/1		368	430	0.63	61	**38**	**407**	**9**	**478**
		1798/2		368	430	0.63	10	**6**	**375**	**2**	**438**
1799	1		372	372	459	0.63	15	**9**	**381**	**2**	**471**
1801	2		735								
		1801/1		367	432	0.63	81	**51**	**418**	**12**	**495**
		1801/2		367	432	0.63	77	**49**	**416**	**12**	**492**
1802	2		746								
		1802/1		373	442	0.63	77	**49**	**421**	**12**	**502**
		1802/2		373	442	0.63	67	**42**	**415**	**10**	**494**
1815	4		1544								
		1815/1		386	453	0.63	54	**34**	**420**	**8**	**495**
		1815/2		386	453	0.63	51	**32**	**418**	**8**	**493**
		1815/3		386	453	0.63	0	**0**	**386**	**0**	**453**
		1815/4		386	453	0.63	0	**0**	**386**	**0**	**453**

SNS NEUTRINO LOAD TABLE NOTES:

- Dead loads (DL) consist of the weight of all construction material.
- Live loads (LL) are produced by the use and occupancy of the building.
- Seismic live load (SLL) is the portion of the live load used for seismic (earthquake) analysis.
- Earthquake (EQ) load is the seismic lateral load due to the motion of the building in the north/south or east/west direction.
- Kip (k) equals 1,000 lbs.
- Kip per square foot (ksf)
- Calculation No. SDE-00-09-28-C-007, Revision 3, May 21, 2002, "Seismic Evaluation of Spallation Neutron Source Target Building – Pile Loads from Gravity and Seismic Motion". Appendix F – Pile Loads from Individual Load Cases. Appendix G – Pile Load Combination Tables.

- Column "a" – Pile cluster node number.
- Column "b" – Number of piles in cluster.
- Column "c" – Individual pile number. See SK-2 for location.
- Column "d" – Total vertical load on pile cluster. 1,500 psf LL is included.
- Column "e" – Total vertical load on individual pile. DL + LL
- Column "f" – Total vertical load on individual pile. DL + SLL + EQ
- Column "g" – Neutrino Uniform DL + LL for Case 1. Load has been distributed at a 2 vertical to 1 horizontal slope and is applied to the piles based on tributary area to each pile. The distribution occurs in the 19 foot thickness of concrete and earth construction, which separates the floor of the enclosure and the top of the piles.
- Column "h" – Tributary area for each pile. See SK-2.
- Column "i" – Load contribution per pile from Neutrino enclosure.
- Column "j" – Total static (vertical) load per pile for DL + LL + Neutrino load
- Column "k" – Additional vertical seismic load per pile from vertical acceleration of the Neutrino enclosure.
- Column "l" – Total vertical seismic load per pile from DL + SLL + EQ + Neutrino Enclosure.